Received 1999 January 27; accepted 1999 September 29
Preprint typeset using LaTeX style emulateapj v. 04/03/99

arXiv:astro-ph/9901388v2 14 Jan 2000

COSMIC CONCORDANCE AND QUINTESSENCE

Limin Wang[1], R. R. Caldwell[2], J. P. Ostriker[3], and Paul J. Steinhardt[2]

Received 1999 January 27; accepted 1999 September 29

ABSTRACT

We present a comprehensive study of the observational constraints on spatially flat cosmological models containing a mixture of matter and quintessence — a time varying, spatially inhomogeneous component of the energy density of the universe with negative pressure. Our study also includes the limiting case of a cosmological constant. We classify the observational constraints by red shift: low red shift constraints include the Hubble parameter, baryon fraction, cluster abundance, the age of the universe, bulk velocity and the shape of the mass power spectrum; intermediate red shift constraints are due to probes of the red shift-luminosity distance based on type 1a supernovae, gravitational lensing, the Lyman-alpha forest, and the evolution of large scale structure; high red shift constraints are based on measurements of the cosmic microwave background temperature anisotropy. Mindful of systematic errors, we adopt a conservative approach in applying these observational constraints. We determine that the range of quintessence models in which the ratio of the matter density to the critical density is $0.2 \lesssim \Omega_m \lesssim 0.5$ and the effective, density-averaged equation-of-state is $-1 \leq w \lesssim -0.2$, are consistent with the most reliable, current low red shift and microwave background observations at the 2σ level. Factoring in the constraint due to the recent measurements of type 1a supernovae, the range for the equation-of-state is reduced to $-1 \leq w \lesssim -0.4$, where this range represents models consistent with each observational constraint at the 2σ level or better (concordance analysis). A combined maximum likelihood analysis suggests a smaller range, $-1 \leq w \lesssim -0.6$. We find that the best-fit and best-motivated quintessence models lie near $\Omega_m \approx 0.33$, $h \approx 0.65$, and spectral index $n_s = 1$, with an effective equation-of-state $w \approx -0.65$ for "tracker" quintessence and $w = -1$ for "creeper" quintessence.

1. INTRODUCTION

The most widely studied cosmological models at the present time are variants of the Cold Dark Matter (CDM) paradigm within which adiabatic perturbations in a dominant CDM species grow due to gravitational instability from quantum fluctuations imprinted during an inflationary era. The bulk of the evidence today strongly favors models within which $\Omega_m < 1$ and any hot component is not significant, $\Omega_{\rm HDM} \ll \Omega_{\rm CDM}$. Several authors (Ostriker & Steinhardt 1995, Krauss & Turner 1995, Turner & White 1997) have found that the best and simplest fit concordant with current observations is provided by

$$\begin{aligned}\Omega_m &= [\Omega_{CDM}] + [\Omega_{baryon}] \\ &\approx [0.30 \pm 0.10] + [0.04 \pm 0.01] \qquad (1)\end{aligned}$$

with $h = 0.65 \pm 0.15$. One is thus led to either an open universe or one in which the remaining energy density required to produce a geometrically flat universe is some additional energy component (E) with

$$\Omega_m + \Omega_E = 1. \qquad (2)$$

An important advantage of the flat model is that it is consistent with standard inflationary cosmology, and its associated resolution of the cosmological horizon and flatness problem and prediction of a nearly scale-invariant spectrum of energy density fluctuations. Finding these arguments compelling[4], we will adopt the ansatz that the universe is spatially flat.

In our previous work (Ostriker & Steinhardt 1995) we identified the range of models consistent with then-current observations, restricting attention to the case where Ω_E is vacuum energy or cosmological constant (Λ). The cosmological constant, a static, homogeneous energy component with positive energy density but negative pressure, was introduced initially by Einstein in a flawed attempt to model our universe as a static spacetime with positive spatial curvature. In a spatially flat universe, however, the negative pressure results in a repulsive gravitational effect which accelerates the expansion of the universe. This earlier analysis, which preceded by several years the recent evidence based on luminosity-red shift surveys of type 1a supernovae, already found that Λ is favored over standard cold dark matter or open models. Over the intervening years, the supernovae measurements as well as other observations have reinforced these conclusions.

In this paper, we update our earlier concordance analysis and expand it to include the possibility that the additional energy component consists of quintessence, a dynamical, spatially inhomogeneous form of energy with negative pressure (Caldwell et al. 1998). A common example

---

[1] Department of Physics, Columbia University, 538 West 120th Street, New York, NY 10027

[2] Department of Physics, Princeton University, Princeton, NJ 08544

[3] Department of Astrophysical Sciences, Princeton University, Princeton, NJ 08544

[4] While inflationary cosmologies can be constructed which lead to a spatially open universe (Gott 1982, and *e.g.* Linde 1999 and references therein), provided careful tuning, choice of inflaton potential, and/or anthropic arguments, we consider here only the standard case of a spatially flat universe.

is the energy of a slowly evolving scalar field with positive potential energy, similar to the inflaton field in inflationary cosmology (Weiss 1987, Ratra & Peebles 1988, Wetterich 1995, Frieman et al. 1995, Coble et al. 1997, Ferreira & Joyce 1997, Caldwell et al. 1998, Zlatev et al. 1998). Unlike a cosmological constant, the dynamical field can support long-wavelength fluctuations which leave an imprint on the cosmic microwave background (CMB) and large-scale structure. In particular, the long wavelength fluctuations change the relation between the amplitude of the CMB anisotropy and the gravitational potential fluctuations so that the COBE normalization of the mass power spectrum depends on the pressure of the quintessence component. A further distinction is that w, the ratio of pressure (p) to energy density (ρ), is $-1 < w \leq 0$ for quintessence whereas w is precisely -1 for a cosmological constant. Hence, the expansion history of the universe for a Λ model versus a quintessence model (for the same Ω_m today, say) is different. In general, the acceleration, the age and the volume of the universe are less for quintessence models than for Λ models (assuming all other cosmic parameters are fixed).

A prime motivation for considering quintessence models is to address the "coincidence problem," the issue of explaining the initial conditions necessary to yield the near-coincidence of the densities of matter and the quintessence component today. For the case of a cosmological constant, the only possible option is to finely tune the ratio of vacuum density to matter-radiation density to 1 part in $\sim 10^{120}$ at the close of inflation in order to have the correct ratio today. Symmetry arguments from particle physics are sometimes invoked to explain why the cosmological constant should be zero (Banks 1996) but there is no known explanation for a positive, observable vacuum density. For quintessence, because it couples directly to other forms of energy, one can envisage the possibility of interactions which may cause the quintessence component to naturally adjust itself to be comparable to the matter density today. In fact, recent investigations (Zlatev et al. 1998, Steinhardt et al. 1999) have introduced the notion of "tracker field" models of quintessence which have attractor-like solutions (Peebles & Ratra 1988, Ratra & Peebles 1988) which produce the current quintessence energy density without the fine-tuning of initial conditions. A related development has been "creeper field" models (Huey & Steinhardt 1999) which are nearly as insensitive to initial conditions but indistinguishable from Λ today.

Fundamental physics provides some further motivation for light scalar fields. Particle physics theories with dynamical symmetry breaking or non-perturbative effects have been found which generate potentials with ultra-light masses which support negative pressure (Affleck et al. 1985, Hill & Ross 1988a, Hill & Ross 1998b, Binetruy et al. 1996, Barreiro et al. 1998, Binetruy 1999). These suggestive results lend appeal to a particle physics basis for quintessence, as a logical alternative to an *ad hoc* invocation of a cosmological constant. We do not aim to base our investigation of the properties of quintessence cosmologies on a specific particle physics model, however, as such models are still in a developmental stage. An intriguing thought is that progress in the cosmological observations and experiments discussed here will soon decide the issue, possibly pointing to new fundamental physics inaccessible in the accelerator laboratory. We would emphasize that scalar field models of quintessence are not only the simplest, well-motivated choice from a particle physics standpoint, but, also, they can mimic fluids with arbitrary equation-of-state. (It was shown explicitly in Caldwell et al. 1998 that there is a one-to-one correspondence between a general time-dependent equation-of-state and an equivalent scalar field potential.) Generalizations to tensor fields or more general stress tensor (Hu 1999) or topological defects (Spergel & Pen 1996) have also been considered; for the purposes of this study based on current observations, they can be well described by scalar fields, in addition.

Extending the realm of cosmological models to include quintessence opens up a new degree of freedom, the equation-of-state of the missing energy component. The added degree of freedom necessarily makes the procedure of selecting viable models more complicated. Previous studies have considered some specific combinations of observations (Silveira & Waga 1997, Turner & White 1997, Garnavich et al. 1998, Perlmutter et al. 1998) or some specific models (Ferreira & Joyce 1997, Ferreira & Joyce 1998). Here we systematically examine the most complete range yet of measures of astrophysical phenomena at low, intermediate, and high red shift and make a complete search in parameter space to objectively identify the viable models. We show that the observations are consistent with Λ and quintessence models for a substantial range of parameters. An impressive feature is how a number of observations, not only the measurements of type 1a supernovae, favor a missing energy component with substantially negative pressure.

The pace of cosmological observations is proceeding so rapidly that any quantitative conclusions may soon become dated. Nevertheless, we think that an assessment at the present time is worthwhile for at least three reasons. First, our study shows a concordance among a growing number of observations. Compared to the previous analysis (Ostriker & Steinhardt 1995) new constraints have been added and old ones have been revised, and, yet, notably, the key conclusions — a new energy component and an accelerating expansion rate — have been significantly strengthened. Second, the study isolates those observations which are playing the lead roles in shaping the current conclusions and identifies observations or combinations thereof which will be most decisive in the near future. Third, this comprehensive analysis enables one to identify specific best-fit models which can be explored in much greater detail to search for more subtle implications and tests.

The organization of the paper is as follows. In section 2, we discuss the parameterization of the cosmological constant and quintessence cosmological models. In section 3, we present the observational constraints, classified by low, intermediate, and high red shift. We evaluate the constraints, presenting the results in section 4. We conclude in section 5 with an identification of the overall best-fit models and a discussion of future observations.

2. PARAMETERIZATION OF QUINTESSENCE COSMOLOGICAL MODELS

The quintessence (QCDM) cosmological scenario is a spatially-flat FRW space-time dominated by radiation at early times, and cold dark matter (CDM) and quintessence (Q) at late times. For simplicity, we will consider models in which the quintessence component consists of a scalar field slowly rolling down its effective potential with a constant equation-of-state. The detailed equations-of-motion are discussed in Caldwell et al. 1998. This class of models is a good approximation for most of the range of quintessence candidates. The models we consider can then be fully characterized by the following five parameters:

$\mathbf{w_Q}$: A constant quintessence equation-of-state, in the range $w \in [-1, 0]$ in the present epoch. In most cases, the quintessence equation-of-state changes slowly with time, but the observational predictions are well approximated by treating w as a constant, equal to

$$\widetilde{w} \approx \int da\, \Omega_Q(a)\, w(a) / \int da\, \Omega_Q(a). \tag{3}$$

We will comment on exceptions later. Tracker field quintessence models have a lower bound on the range of w, while creeper quintessence leads to w very close to -1, which is effectively indistinguishable from a true cosmological constant.

$\mathbf{\Omega_m}$: The matter density parameter, defined as the ratio of the matter energy density, including CDM and baryons, to the critical energy density $\rho_c = 3H^2/8\pi G$, where H is the Hubble constant. We assume that any contribution to the energy density due to a hot component, such as neutrinos, is small, insofar as free-streaming has a negligible effect on the clustering of CDM. Unless otherwise specified, we have imposed $\Omega_m + \Omega_Q = 1$, where Ω_Q is the corresponding density parameter for quintessence. Hence, the matter density parameter lies in the range $\Omega_m \in [\Omega_b, 1]$.

$\mathbf{\Omega_b}$: The baryon density parameter, defined as the ratio of the baryonic energy density to the critical energy density.

h: The Hubble parameter, related to the Hubble constant by $H = 100\, h$ km/s/Mpc.

$\mathbf{n_s}$: The index of the power spectrum of primordial density fluctuations in the matter and radiation. This parameter also controls the contribution of tensor perturbations, for which we consider two cases. In the first case, we impose the inflationary relation between the amplitude of the primordial density and gravitational wave (tensor) perturbations for $n_s \leq 1$, revised for the case of quintessence (Caldwell & Steinhardt 1998). For $n_s > 1$, we assume the tensor contribution is negligible. In the second case, we assume the tensor contribution is negligible for all values of the spectral index. (We only illustrate the first case; the second case yields an indistinguishable result in regard to our concordance analysis.)

The most revealing way to depict the concordance of constraints on quintessence models is to project the five-dimensional parameter space into the Ω_m-w plane. In displaying this plane, we assume the universe is spatially flat. Since the flatness condition requires $\Omega_Q = 1 - \Omega_m$, the parameters w and Ω_m completely specify the quintessence portion of the cosmology. ΛCDM corresponds to the line $w = -1$, and SCDM corresponds to the line $\Omega_m = 1$ in this plane.

3. OBSERVATIONAL CONSTRAINTS

We take a conservative approach in applying the cosmological constraints. Observational cosmology is currently in a period of rapid growth so that the current constraints must be considered as *work in progress*, rather than final. Certainly, measurements of many astrophysical phenomena are becoming more refined, with greater precision as statistical errors are reduced, and with greater accuracy as systematic errors are better understood. If this situation described all observations, we could confidently apply the results to the full limits of the published errors. Because the observational constraints typically restrict combinations of independent model parameters, then by combining several experimental results, we could find tighter parameter bounds than if the observations were applied individually. For example, combining two constraints restricts a two-parameter system to an ellipse in parameter space, whereas the individual constraints applied successively allow a rectangle which contains that ellipse. The former combination would allow the determination of a model which was "best" in the maximum likelihood sense. However, not all measurements have well controlled systematic errors or even high precision statistical errors. Nor do they have true gaussian errors. Nor are the errors uncorrelated. A prime example is the current set of type 1a supernovae magnitude-red shift data, which must be interpreted with caution. For these reasons, we do not advocate cosmological parameter extraction with the current set of astrophysical data. Until the coming generation of precision experiments are on-line, we believe it can be misleading to combine the full set of astrophysical data as if the errors were statistical and gaussian.

For this reason, we employ an additional procedure, which we call "concordance," to evaluate the observational constraints. We identify models as passing the observational constraints if they lie within 2σ of each individual constraint. (We do not consider the joint probabilities spanning two or more observations.) We allow a generous range for systematic errors. Not only does this procedure provide a reliable picture of current constraints, but there is the added advantage that it renders transparent which observations are most important in delimiting the range of currently allowed parameters and which future observations will be most influential.

One might characterize the difference between the two approaches as follows: two identical and observationally independent constraints on a single parameter do not change, at all, the allowed range of that parameter in the concordance analysis, but do reduce the range in a maximum likelihood approach. Clearly, the concordance approach is too conservative if the errors are known to be gaussian. However, in the current case, systematics dominate and the correlations between errors in different observations is unclear. In these circumstances, as discussed in the Appendix, the maximum likelihood approach can produce seriously misleading results. One should be especially watchful and examine closely situations where the concordance and maximum likelihood analyses strongly disagree. Maximum likelihood has the undesireable feature that it will seek a compromise among conflicting data. Hence, we advocate the more conservative concordance approach, supplemented with comparison to a full maximum likelihood estimator for the constraints assuming gaussian errors.

We classify the observations by red shift. At low red shift, $z \ll 1$, the constraints are due to: the Hubble constant; age of the universe; baryon density; x-ray cluster abundance; shape of the mass power spectrum; and bulk flow. At intermediate red shift, $z \sim 1$, the constraints are due to: type 1a supernovae; evolution of the x-ray cluster abundance; gravitational lensing; Lyman-α forest. At high red shift, $z \gg 1$, the constraints are due to: the fluctuation amplitude and spectral tilt based on the large angle CMB temperature anisotropy (COBE); small angle CMB temperature anisotropy. The high red shift CMB constraint due to COBE, along with the set of low red shift results, serve as the strongest, most reliable constraints. These constraints will be shown to dominate the boundary of the allowed parameter range. The intermediate red shift constraints, due to SNe and the evolution of x-ray clusters, are rapidly reaching the point where they impact the range of cosmological models. The small angle CMB measurements, as well, are soon to yield prime cosmological information. We will consider each of these constraints in turn.

The observational constraints used to restrict the quintessence parameter space are listed in the following subsection. The low red shift, and COBE-based high red shift constraints compose the core set of concordance tests of our cosmological models. The remaining intermediate and high red shift constraints are less certain at the present, although they offer the promise of powerful discrimination between models in the near future.

3.1. *Low Redshift*

H: The Hubble constant has been measured through numerous techniques over the years. Although there has been a marked increase in the precision of extragalactic distance measurements, the accurate determination of H has been slow. The H_0 Key Project (Freedman et al. 1998), which aims to measure the Hubble constant to an accuracy of 10%, currently finds $H = 73 \pm 6(\mathrm{stat}) \pm 8(\mathrm{sys})$ km/s/Mpc; the method of type 1a supernovae gives $H = 63.1 \pm 3.4(\mathrm{internal}) \pm 2.9(\mathrm{external})$ km/s/Mpc (Hamuy et al. 1996); a recent measurement based on the Sunyaev-Zeldovich effect in four nearby clusters gives $H = 54 \pm 14$ km/s/Mpc (Myers et al. 1997); typical values obtained from gravitational lens systems are $H \sim 50-70$ km/s/Mpc with up to $\sim$ 30% errors (Falco et al. 1997, Keeton & Kochanek 1997, Kundic et al. 1997, Schechter et al. 1997). Using surface brightness fluctuations to calibrate the bright cluster galaxy Hubble diagram, a far-field value $H = 89 \pm 10$ km/s/Mpc, out to $\sim 11,000$ km/s, has been obtained (Lauer et al. 1998). Clearly, convergence has not yet been reached, although some methods are more prone to systematic uncertainties. Based on these diverse measures, our conservative estimate for the Hubble parameter is $H = 65 \pm 15$ km/s/Mpc at effectively the 2σ level. While knowledge of H would certainly be a decisive constraint, our current uncertainty will not prevent us from narrowing the field of viable cosmological models.

$\mathbf{t_0}$: Recent progress in the dating of globular clusters and the calibration of the cosmic distance ladder has relaxed the lower bound on the age of the universe. We adopt $t_0 \geq 9.5$ Gyr as a 95% lower limit (Chaboyer et al. 1998, Salaris & Weiss 1998), although we note that some arguments (Paczynski 1999) suggest a 10% higher limit is more appropriate.

BBN: Recent observations of the deuterium abundance by Burles and Tytler yield $D/H = 3.4 \pm 0.3(\mathrm{stat}) \times 10^{-5}$ (Burles & Tytler 1997a, Burles & Tytler 1997b, Burles & Tytler 1998). If this value reflects the primordial abundance, then big bang nucleosynthesis (BBN; for a review see Schramm & Turner 1998 and references therein) with three light neutrinos gives $\Omega_b h^2 = 0.019 \pm 0.002$, where the 1σ error bars allow for possible systematic uncertainty. While other observations suggest that the abundance varies on galactic length scales where it is expected to be uniform, suggesting that heretofore unknown processes may be processing the deuterium (Jenkins et al. 1999), we will adopt the hypothesis that the cosmological abundance has been ascertained by the measurements of Burles & Tytler.

BF: Observations of the gas in clusters have been used to estimate the baryon fraction (compared to the total mass) to be $f_{gas} = (0.06 \pm 0.003)h^{-3/2}$ (Evrard 1997; also see White et al. 1993, Fukugita et al. 1997). The stellar fraction is estimated to be less than 20% of the gas fraction, so that $f_{stellar} = 0.2h^{3/2} f_{gas}$. Next, simulations suggest that the baryon fraction in clusters is less than the cosmological value by about 10% (Lubin et al. 1996) representing a depletion in the abundance of baryons in clusters by a factor of 0.9 ± 0.1. Hence, the cosmological baryon fraction (Ω_b/Ω_m) is estimated to be $f_{baryon} = (0.067 \pm 0.008)h^{-3/2} + 0.013$ at the 1σ level. Using the observed baryon density from BBN, we obtain a constraint on Ω_m:

$$\Omega_m = \frac{0.019h^{-2}}{0.067h^{-3/2} + 0.013}\Big(1 \pm 0.32\Big) \tag{4}$$

at the 2σ level. For $h = 0.65$, this corresponds to a value of $\Omega_m = 0.32 \pm 0.1$.

The baryon fraction has also been estimated on smaller scales such as galaxy systems (see McGaugh 1998 and references therein). However, the relationship between the local baryon fraction on those scales and the global baryon fraction is uncertain and currently beyond the power of numerical study.

$\boldsymbol{\sigma_8}$: The abundance of x-ray clusters at $z = 0$ provides a model dependent normalization of the mass power spectrum at the canonical $8h^{-1}$ Mpc scale. The interpretation of x-ray cluster data for the case of quintessence models has been carried out in detail in Wang & Steinhardt 1998, in which case the constraint is expressed as

$$\sigma_8 \Omega_m^{\gamma} = (0.5 - 0.1\Theta) \pm 0.1 \tag{5}$$

where the error bars are 2σ, with

$$\begin{aligned} \gamma &= 0.21 - 0.22w + 0.33\Omega_m + 0.25\Theta \\ \Theta &= (n_s - 1) + (h - 0.65). \end{aligned} \tag{6}$$

This fitting formula is valid for the range of parameters considered in this paper.

Perhaps the two most important constraints on the mass power spectrum at this time are the COBE limit on large scale power and the cluster abundance constraint which fixes the power on $8h^{-1}$ Mpc scales. Together, they fix the spectral index and leave little room to adjust the power spectrum to satisfy other tests.

Shape: If light traces mass with a constant bias factor on large scales, then the deprojected APM galaxy cluster data (Peacock 1997b) can be used to constrain the shape of the underlying mass power spectrum. The bias factor is defined as $b^2 \equiv P_{APM}/P_{mass}$, the ratio of the APM to mass power spectra on a given scale; we assume the bias represents a constant, quadratic amplification of the clustering power of rare objects over the density field on large scales (Kaiser 1986). Hence, in keeping with our spirit of conservativism, we restrict our attention to wavenumbers which are well within the linear regime, using only the seven lowest frequency bins (as given in Peacock 1997a) for scales above 8 Mpc/h. The shape constraint consists of the requirement that the mass power spectrum fit the seven APM data points with $b \geq 1$ and a reduced $\chi^2 \leq 2.0$, corresponding to a confidence level of 95%. In effect, our shape test depends also on the power spectrum amplitude. The lower bound on the bias is due to the assumption that the bright, luminous APM objects are preferentially formed in highly overdense regions (Davis et al. 1985, Bardeen 1986, Kaiser 1986, Cen & Ostriker 1998, Blanton et al. 1998). (Although the bias may be very large at the time of formation, simple arguments indicate that by the present time, b may have decreased to no lower than unity. See Fry 1986, Tegmark & Peebles 1998). The consequences of $b < 1$ will be discussed. While we give no upper bound on b, almost all the best fitting values for concordance models fall within the rough (model-dependent) upper bound estimate of $b \lesssim 1.5$ based on higher-order statistics of the APM data set and current theoretical *ab initio* modeling (Gaztanaga & Frieman 1994, Cen & Ostriker 1998, Blanton et al. 1998). Our computations show that the popular "shape parameter" $\Gamma \equiv \Omega_m h$ is not an accurate description of the goodness of fit to the APM data, given the variety of models that we consider here, since the amplitude of the power spectrum is characterized by other combinations of parameters, including w. As illustrated in Figure 1, five sample models with Γ ranging from 0.20 to 0.52 all pass our shape test based on a χ^2 analysis.

Velocity Field: The large-scale velocity field has long been used as a means to probe the background and fluctuation matter density field. One method is to compare peculiar velocity data obtained from distance indicators, such as Tully-Fisher, and from red shift surveys, in order to estimate Ω_m, modulo an assumption about biasing. Through this method, the quantity $\beta \equiv f(\Omega_m)/b$ is obtained, where $f \equiv d\ln\delta_m/d\ln a \sim \Omega_m^{0.6}$ and b is a linear bias parameter. A variety of recent results (Davis, Nusser, & Willick 1993, Willick et al. 1997, Willick & Strauss 1997, da Costa et al. 1998) find $\beta \sim 0.5 - 0.6$. For a bias not too different from unity, these results suggest a low matter density. In the lack of a more complete understanding of bias, however, this method cannot be transformed into a rigorous constraint on Ω_m. As well, it remains to be understood why similar approaches which compare the density fields obtained from distance indicators and red shift survey data, along the lines of the POTENT method (Bertschinger & Dekel 1989), generally obtain higher values, *e.g.* $\beta \sim 0.9$ (Sigad et al. 1998). Another method is to compare observations with the predicted velocity field within the context of a particular cosmological model. Results based on the Mark III (Zaroubi et al. 1997) and SFI (Zehavi 1998, Freudling et al. 1999) catalogs yield the constraint $f^2P(k) = (4.8 \pm 1.5) \times 10^3\,(\mathrm{Mpc/h})^3$ and $(4.4 \pm 1.7) \times 10^3\,(\mathrm{Mpc/h})^3$ at $k = 0.1\,\mathrm{h/Mpc}$, respectively. Extrapolating to smaller scales, within the class of ΛCDM models, the SFI constraint can be recast as $\sigma_8 f = 0.82 \pm 0.12$. Due to the discrepancy with the cluster abundance constraint, we are hesitant to apply this recent result until further analysis reinforces its conclusions.

The bulk flow on the largest scales provides another method to do cosmology with the velocity field. In Figure 2 we compare the predictions of a set of QCDM models with observation. The large sample variance on the Maxwellian distributed velocity field means that consistency requires the observations lie below the upper 95%CL bulk velocity. (The lower 95%CL bulk velocity is very small, so we may effectively treat this constraint as an upper bound.) A measurement near or above the swath of predicted curves could serve as a strong indicator of the cosmology. For comparison, we also show the measured bulk velocities of Dekel et al. 1999, Giovanelli et al. 1998, and Lauer & Postman 1994. At present, the diversity of measurements, as displayed in Figure 2, dilutes the strength of the constraint resulting from the comparison of the velocity dipole with the CMB dipole.

3.2. *Intermediate Redshift*

SNe: Type 1a supernovae are not standard candles, but empirical calibration of the light curve - luminosity relationship suggests that the objects can be used as distance indicators. There has been much progress in these observations recently, and there promises to be more. Hence, a definitive constraint based on these results would be premature. However, we examine the recent results of the High-Z Supernova Search Team (HZS: Riess et al. 1998, Garnavich et al. 1998) and the Supernova Cosmology Project (SCP: Perlmutter et al. 1998) to constrain the luminosity distance - red shift relationship in quintessence cosmological models. We have adopted the following data analysis procedure: we use the supernova data for the shape of the luminosity - red shift relationship only, allowing the calibration, and therefore the Hubble constant, to float; we excise all SNe at $z < 0.02$ to avoid possible systematics due to local voids and overdensities; for SNe at $z > 0.02$, we assume a further uncertainty, added in quadrature, corresponding to a peculiar velocity of 300km/s in order to devalue nearby SNe relative to the more distant ones (for the SCP data, a velocity of 300km/s has already been included). There is substantial scatter in the supernovae data, as seen in Figure 3. The scatter is so wide that no model we have tested passes a χ^2 test with the full SCP data set; using a reduced set, Fit C, argued by the SCP as being more reliable Perlmutter et al. 1998, a finite range of models do pass the χ^2 test and the range is comparable to the range obtained by the χ^2 test using the HZS data set. To gauge the current situation, we will report both χ^2 tests and maximum likelihood tests; to be conservative, we use the largest boundary (the χ^2 test based on HZS data using MLCS analysis) for our concordance constraint.

Cluster Evolution: The abundance of rich clusters — objects presumed to have formed from high density peaks drawn from the exponential tail of an initially Gaussian perturbation distribution – can be used to constrain the amplitude of the mass power spectrum at intermediate red shift. The current observations have been converted into a number density of clusters above a certain mass threshold

$M_{1.5}$, defined to be the mass within the comoving radius $R_{com} = 1.5h^{-1}$ Mpc. For the models of interest, the abundance evolves approximately as a power law for $0 < z < 1$:

$$n(> M_{1.5}, z) \propto 10^{A(M_{1.5})z} \tag{7}$$

(see Wang & Steinhardt 1998). The bigger $A(M_{1.5})$ is, the weaker the evolution is, implying low Ω_m and w. Since the measurements (summarized in Bahcall et al. 1997) are still in the preliminary stage, we adopt $A(M_{1.5} = 8 \times 10^{14}h^{-1}\mathrm{Mpc}) = -1.7^{+1.5}_{-2.1}$ as a conservative, 2σ limit. Similar tests have been applied in the context of ΛCDM and open models (Bahcall et al. 1997, Carlberg et al. 1997), for which the results are model dependent.

Lensing Counts: The statistics of multiply imaged quasars, lensed by intervening galaxies or clusters, can be used to determine the luminosity distance - red shift relationship, and thereby constrain quintessence cosmological models. There exists a long literature of estimates of the lensing constraint on Λ models (e.g. from Turner et al. 1984 to Falco et al. 1998). In one approach, the cumulative lensing probability for a sample of quasars is used to estimate the expected number of lenses and distribution of angular separations. Using the Hubble Space Telescope Snapshot Survey quasar sample (Maoz et al. 1993), which found four lenses in 502 sources, Maoz-Rix (Maoz & Rix 1993) arrived at the limit $\Omega_\Lambda \lesssim 0.7$ at the 95% CL. In a series of studies, similar constraints have been obtained using optical (Kochanek 1995, Kochanek 1996) and radio lenses (Falco et al. 1998). Waga and collaborators (Torres & Waga 1996, Waga & Miceli 1999) have generalized these results, finding that the constraint weakens for larger values of the background equation-of-state, $w > -1$ (as noted earlier by Ratra & Quillen 1992). In our evaluation of the constraint based on the HST-SSS data set, we find that the 95% confidence level region is approximately described by $\Omega_Q \lesssim 0.75 + (1 + w)^2$, until the inequality is saturated at $w = -1/2$, consistent with Torres & Waga 1996, Waga & Miceli 1999. In principle, this test is a sensitive probe of the cosmology; however, it is susceptible to a number of systematic errors (for a discussion, see Malhotra et al. 1997, Cheng & Krauss 1999). Uncertainties in the luminosity function for source and lens, lens evolution, lensing cross section, and dust extinction for optical lenses, threaten to render the constraints compatible with or even favor a low density universe over $\Omega_m = 1$. Taking the above into consideration, none of the present constraints on quintessence due to the statistics of multiply imaged quasars are prohibitive: models in concordance with the low-z constraints are compatible with the lensing constraints.

Ly-α (and other mass power spectrum measurements at moderate red shift, $1 < z < 10$): The Ly-α forest has been used as the basis of a number of cosmological probes. Most recently, the effect of the local mass density in the intergalactic medium on the Ly-α optical depth (Hui 1999, Croft et al. 1998a) has been used to estimate the mass power spectrum at a red shift of $z = 2.5$ (Croft et al. 1998b, Weinberg et al. 1998). This is a good pedagogical example to study what can and cannot be learned from studies at moderate red shift $1 < z < 10$. In Figure 4 we show the linear mass power spectrum today (upper panel) and at red shift $z = 2.5$ (lower panel) for the representative best-fit models discussed in Table I. The mass power spectra in the upper panel all satisfy COBE normalization at large scales and the cluster abundance constraint on σ_8 on 8 h^{-1} Mpc scales. Since the models have already passed the constraints on 8 h^{-1} Mpc scales and higher, one might hope that tests of the linear power spectrum at smaller scales might further distinguish the models. However, smaller scales correspond to the non-linear growth regime where effects like scale-dependent bias make it difficult to compare observations to the linear power spectrum. Measurements of the Lyman-α forest are promising because they probe the power spectrum on smaller scales at a red shift before non-linearities develop and, hence, enable direct comparison to the linear power spectrum. We draw the reader's attention to the fact that, in converting to $z = 2.5$, we have made a model-dependent rescaling of the abscissa so that the units are those of velocity, which then allows direct comparison to the data. In the upper ($z = 0$) panel, the models differ substantially on large scale but appear to converge on small scales. Projecting back to $z = 2.5$ and rescaling, one might hope that the models are distinct due to the differing growth functions. However, instead, examples with the same spectral tilt and $\Omega_m H_0/H(z)$ (as is demonstrated inadvertently by our representative models) nearly overlap everywhere, making discrimination very difficult. When $\Omega_m H_0/H(z)$ is fixed, as shown in the figure, then, we note, the Lyman-α measurements can be used to determine the tilt, n_s.

The current data appears to favor $n_s = 1$. There is some hope that improved limits can discriminate among models with different tilt, but determining other parameters, and especially discriminating between cosmological constant and quintessence on this basis, appears hopeless because the predictions of various models converge, as shown in the lower panel. Of course, this conclusion applies not only to Lyman-α forest measurements, but any approach that measures the mass power spectrum at moderate red shift.

Further applications of the Ly-α forest, such as the abundance of damped Ly-α absorbers (Gardner et al. 1997) and correlations in the lines of sight at red shifts $z \sim 2 - 4$ (McDonald & Miralda-Escude 1998, Hui et al. 1999) have been developed as tests of geometry and expansion history, although no substantial constraints have as yet been obtained.

There are a number of observational probes which are sensitive to the cosmology, but which have not yet matured into critical tests. We list some of these tests which may prove to be powerful constraints in the near future. Measures of the abundance of objects, similar to the cluster evolution constraint, can be used to gauge the growth of structure. Observations of galaxies formed as early as $z \gtrsim 3$ (Steidel et al. 1998) have been interpreted, on the basis of a Press-Schechter formalism (Press & Schechter 1974), to suggest that among a family of CDM cosmologies, flat, low-density models best satisfy the constraint (Mo & Fukugita 1996).

Finally, it has been proposed to use the statistics of gravitational lens arcs produced by intermediate red shift clusters as a means to distinguish cosmological models (Wu & Mao 1996, Bartelmann et al. 1998). These are potentially extremely powerful tests, insofar as the rare, high density fluctuations reflect the underlying cosmology. In particular, the lens arcs statistics are exponentially sensitive to the growth function, which differs for Λ versus quintessence models and, hence, has the potential of distinguishing the two scenarios. However, results based on numerical simulations are not yet capable of resolving the core of clusters accurately enough to provide reliable limits (Wambsganss et al. 1998) from the theoretical side.

3.3. *High Redshift*

One of the most powerful cosmological probes is the CMB anisotropy, an imprint of the recombination epoch on the celestial sphere. The large angle temperature anisotropy pattern recorded by COBE can be used to place two constraints on cosmological models.

COBE norm: The observed amplitude of the CMB power spectrum is used to constrain the amplitude of the underlying density perturbations. We adopt the method of Bunn & White 1997 to normalize the power spectrum to COBE. As we use a modified version of CMBFAST (Seljak & Zaldarriaga 1996) to compute the CMB anisotropy spectra, this normalization is carried out automatically.) We have verified that this method, originally developed for Λ and open CDM models, can be applied to the quintessence cosmological models considered in this work (Dave 1998). Of course, there is uncertainty associated with the COBE "normalization": the 2σ uncertainty in rms quantities is approximately 20% (see footnote #4 in Bunn & White 1997), which conservatively allows for statistical errors, as well as the systematic uncertainty associated with the differences in the galactic and ecliptic frame COBE map pixelizations, and potential contamination by high-latitude foregrounds(*e.g.* Gorski et al. 1998).

$\mathbf{n_s}$: COBE has been found to be consistent with a $n_s = 1.2 \pm 0.3$ spectral index (Gorski et al. 1996, Hinshaw et al. 1996), but this assumes the only large angular scale anisotropy is generated via the Sachs-Wolfe effect on the last scattering surface. This neglects the baryon-photon acoustic oscillations, which produce a rise in the spectrum, slightly tilting the spectrum observed by COBE. In general, the spectral index determined by fitting the large angular scale CMB anisotropy of a quintessence model, which is also modified by a late-time integrated effect, to the shape of the spectrum tends to overestimate the spectral tilt. For example, analysis of a class of CDM models (Hancock et al. 1998) (ΛCDM and SCDM, a subset of the models considered here) finds a spectral tilt $n_s = 1.1 \pm 0.1$. We conservatively restrict the spectral index of the primordial adiabatic density perturbation spectrum, with $P(k) \propto k^{n_s}$, to lie in the interval $n_s \in [0.8, 1.2]$. Note that inflation generically predicts $n_s \sim 1$, with n_s slightly less than unity preferred by inflaton potentials which naturally exit inflation.

Small Angle CMB: Dramatic advances in cosmology are expected in the near future, when the MAP and Planck satellites return high resolution maps of the CMB temperature and polarization anisotropy. When the measurements are analyzed, we can expect that the best determined cosmological quantities will be the high multipole C_ℓ moments, such that any proposed theory must first explain the observed anisotropy spectrum. At present, however, there is ample CMB data which can be used to constrain cosmological models.

We take a conservative approach in applying the small angular scale CMB data as a model constraint. Our intention is to simply determine which quintessence models are consistent with the ensemble of CMB experiments, rather than to determine the most likely or best fitting model; examining Figure 5, the error bars are clearly so large that a 'best fit' has little significance. We have restricted our attention to that subset of published CMB experimental data which satisfies the following objective criteria: multifrequency; positive cross-correlation with another experiment; careful treatment of foregrounds. (While we advocate these criteria, our conclusions are not strongly sensitive to this selection of data.) Hence, we use the bandpower estimates from COBE (Bennett et al. 1996), Python (Platt et al. 1997), MSAM (Cheng et al. 1997), QMAP (Devlin et al. 1998, Herbig et al. 1998, Oliveira-Costa et al. 1998), Saskatoon (Netterfield et al. 1997), CAT (Scott et al. 1996), and RING5M (Leitch et al. 1998) experiments as the basis of the small angle CMB cosmological constraint. Figure 5 shows the bandpower averages at the effective multipole number, l_e, with several QCDM models for comparison. We apply a simple χ^2 test with the predicted bandpower averages, δT_{l_e} (defined in Bond 1995). (A compilation of bandpower averages and window functions is available from Knox[5] and Tegmark[6].) Since the reported bandpower errors are typically not Gaussian distributed, treating the δT_{l_e} as a Gaussian random variable can introduce a bias in the estimation of the quality of agreement. In this case, we also consider a χ^2 test in the quantity $\ln(\delta T^2_{l_e})$, following Bond et al. 1998.

Figure 5 illustrates features relevant to limits on the spectral index, n_s. The COBE limit on the spectral index is reported to be $n_s = 1.2 \pm 0.3$ (Gorski et al. 1996, Hinshaw et al. 1996) based on comparison between data and standard CDM models. In the Figure, though, it is apparent that there is negligible difference in the low angular scale predictions despite a range of $\Delta n = 0.2$. The difference in the large angular scale integrated Sachs-Wolfe contribution compensates for the difference in spectral index. Hence, as will be addressed in a later paper, the COBE limit on n_s is somewhat expanded when QCDM is included.

4. CONCORDANCE RESULTS

We have evaluated the cosmological constraints for the set of quintessence models occupying the five dimensional parameter space: w, Ω_m, Ω_b, h, n_s. The results are best represented by projecting the viable models onto the $\Omega_m - h$ and $\Omega_m - w$ planes.

The concordance region due to the suite of low red shift constraints, including the COBE normalization and tilt n_s, are displayed in Figures 6, 7. Each point in the shaded region represents at least one model in the remaining three dimensional parameter space which satisfies the observational constraints.

In Figure 6, the boundaries in the Ω_m direction are determined by the combined BBN and BF constraints as a function of h, while h is only restricted by our conservative allowed range and the age constraint. The age does not impact the $\Omega_m - h$ concordance region, since for the allowed values of Ω_m and h, there is always a model with a sufficiently negative value of w to satisfy the age constraint. Relaxing either the BBN or BF constraint would raise the upper limit on the matter density parameter to allow larger values of Ω_m. This requires a simultaneous reduction in the spectral index, n_s, in order to satisfy both the COBE normalization and cluster abundance.

---

[5] www.cita.utoronto.ca/∼knox/radical/bpdata.html

[6] www.sns.ias.edu/∼max/cmb/experiments.html

In Figure 7, the upper and lower bounds on Ω_m are again determined by the combination of BBN, BF, and h. The lower bound on Ω_m due to the combination of the BBN and BF constraints can be relaxed if we allow a more conservative range for the baryon density, such as $0.006 < \Omega_b h^2 < 0.022$ (Levshakov 1998, Olive, Steigman & Walker 1999). However, the constraints due to σ_8 and the shape of the mass power spectrum take up the slack, and the lower boundary of the concordance region is relatively unaffected. The lower bound on Ω_m near $w = -1$ is determined in part by the shape test; the mass power spectrum in a model with low Ω_m and strongly negative w is a poor fit to the shape of the APM data, based on a χ^2-test. This constraint on models near $w = -1$ is relaxed if we allow anti-bias ($b < 1$), although $b < 1$ is strongly disfavored on a theoretical basis. At the other end, for $w \gtrsim -0.6$, the lower bound on Ω_m is determined by the combination of the upper bound on the spectral index, and the x-ray cluster abundance constraint on σ_8. If we further restrict the bias to $b < 1.5$, a small group of models at the upper right corner with $w \gtrsim -0.2$ and $\Omega_m \gtrsim 0.4$ will fail the shape test.

We see that models occupying the fraction of the parameter space in the range $-1 \leq w \lesssim -0.2$ and $0.2 \lesssim \Omega_m \lesssim 0.5$ are in concordance with the basic suite of observations, suggesting a low density universe. It is important to note that the set of viable models spans a wide range in w; the concordance region is not clustered around $w = -1$, or Λ, but allow such diverse behavior as $w \sim -1/3$. However, the case $w = 0$, which can result from the scaling exponential potential (Ratra & Peebles 1988, Peebles & Ratra 1988), is clearly in contradiction with observation: the Ω_m required by the x-ray cluster abundance constraint is incompatible with the matter density parameter allowed by the BF and BBN constraints. Hence, the models with $w = 0$ explored in Ferreira & Joyce 1997, Ferreira & Joyce 1998 are not viable.

We have taken the attitude in our work that current observational uncertainties are dominated by systematic errors, so that a conservative method of combining observational constraints is by concordance. We apply the 2σ limits for each individual observation to pare down the viable parameter range. However, it is interesting to compare this to what a naive maximum likelihood estimate (treating the errors as gaussian) would give. In Figure 8 we show the 2σ contour in the $\Omega_m - w$ plane, where the remaining parameters have been marginalized. This parameter region is only slightly smaller than that resulting from concordance. It is reassuring that this technique yields approximately the same result, although one should be cognizant of some of the pitfalls of both methods as discussed in the Appendix. In using the maximum likelihood technique, we lose some of our ability to identify the constraint dominating a particular portion of the contour. However, we show that by lifting the shape test, the constraint relaxes on the range of Ω_m allowed for models with w closer to -1, including ΛCDM. For the sake of argument, the 'best fit' models, where the likelihood is maximized, are also shown. We see more clearly that the shape test drives the preferred models away from $w = -1$, towards $w \sim -1/2$.

The concordance approach offers no such 'best fit', as it contains no procedure for weighting or combining data. However, in Figure 9 we carry out the exercise of artificially shrinking all the error bars, to find the last remaining models. This is equivalent to imagining that all measurements have accurately determined the intended quantity, but overstated their uncertainties. This procedure narrows down to the same set of models, $\Omega_m \sim 0.33$, but is not driven as strongly by the shape test as is the maximum likelihood procedure.

The most potent of the intermediate red shift constraints is due to type 1a supernovae, which we present in Figure 10. In addition to the SCP results, the HZS group has presented two different analyses of their catalog of SNe, based on multi-color light curve shapes (MLCS) and template fitting; hence we show three SNe results. Carrying out a maximum likelihood analysis, all three give approximately the same result for the location of the 2σ bound, favoring concordant models with low Ω_m, and very negative w. It is interesting to observe that the SNe bound is consistent with the core of the low red shift concordance region, displayed earlier in Figure 9. Based on the SCP maximum likelihood analysis, Perlmutter et al. 1999 have reported a limit $w \leq -0.6$ at the 1σ level. A χ^2 analysis of the same data gives a somewhat different result: the Fit C SCP data and the HZS data sets give comparable, although weaker, results to the likelihood analysis. In the spirit of conservativism, we have used the weakest bound which we can reasonably justify. Hence, for the concordance analysis, we use the 2σ contour resulting from a χ^2 test.

The statistical rate of gravitational lensing provides a counter to the trend towards low matter density. In Figure 11 we present the results of our analysis of the HST-SSS lenses. Other groups have come to similar conclusions, based on this and other lens surveys. Our results are in excellent agreement with Torres & Waga 1996, Waga & Miceli 1999, as well as the more sophisticated analyses carried out by Maoz & Rix 1993, Kochanek 1995, Kochanek 1996, Falco et al. 1998 for ΛCDM. In general, there are fewer lenses observed than expected based on the volume-red shift relation for a low density, Λ-dominated universe. The disparity between theory and observation is reduced as the matter density increases, or as w increases.

We have evaluated the x-ray cluster evolution constraint using the observed abundance of rich clusters at $z \sim 1$. This test constrains the amplitude of mass fluctuations and the rate of perturbation growth. While it has been argued that this reduces to a bound on σ_8 for ΛCDM models (Bahcall & Fan 1998), it has been shown that the bound depends on w for QCDM scenarios by Wang & Steinhardt 1998. In Figure 12 we show the consequence of the cluster evolution constraint on the concordance models in the $\Omega_m - w$ plane; at this stage, the early formation of structure implied by the observations argues against concordant quintessence models with an equation-of-state $w \gtrsim -0.3$. When the measurements comprising this constraint improve, we can expect a much more stringent result. Considering the hypothetical situation that future observations successfully reduce the systematic uncertainty to the present 1σ level, the constraint boundary would shift to the small region with $-0.8 \lesssim w \lesssim -0.5$ and $0.25 \lesssim \Omega_m \lesssim 0.3$.

We have evaluated the high red shift constraint due to the select ensemble of CMB anisotropy measurements, using the COBE, Python (Platt et al. 1997), MSAM (Cheng et al. 1997), QMAP (Devlin et al. 1998, Herbig et al. 1998, Oliveira-Costa et al. 1998), Saskatoon (Netterfield et al. 1997), CAT (Scott et al. 1996), and RING5M (Leitch et al. 1998) results. Based on a χ^2 test in δT_l, the set of concordant models projected down to the $\Omega_m - h$ and $\Omega_m - w$ planes is unchanged from the low red shift concordance region at even the 1σ level. This "null" result from the CMB should not be too surprising; the current observational data is capable only of discerning a rise and fall in power in the C_ℓ spectrum across $\ell \sim 100 - 300$. The results are unchanged if we include additional current CMB results, or use a χ^2 test in $\ln(\delta T_l^2)$, as suggested in Bond et al. 1998. Rather, we must wait for near-future experiments which have greater $\ell-$coverage, *e.g.* BOOMERANG, MAT, and MAXIMA, which are expected to significantly reduce the uncertainties.

Since the submission of this manuscript, the data from the MAT (Miller et al, 1999) and BOOMERANG (Mauskopf et al, 1999) experiments have been released. However, neither significantly changes our results.

Thus far we have applied the low red shift constraints in sequence with one of the other intermediate or high red shift constraints. It is straight forward to see how the combined set of constraints restrict the quintessence parameter space. Taking the low red shift constraint region, which is shaped primarily by the BF, BBN, H, and σ_8 constraints, the dominant bounds on the $\Omega_m - w$ plane are then due to SNe and lensing. The SNe drives the concordance region towards small Ω_m and negative w; the lensing restricts low values of Ω_m. Putting these all together, an ultimate concordance test is presented in Figure 13. We see that the resulting concordance region in the $\Omega_m - w$ plane is very similar to the core region obtained in Figure 9. If the present observations are reliable, we may conclude that these models are the most viable among the class of cosmological scenarios considered herein.

It is beyond the scope of the present work to determine how well future observations will determine the values of cosmological parameters in a QCDM scenario. However, we are in a position to highlight those observations which appear well suited to testing the quintessence hypothesis. Clearly, the first goal must be to distinguish Q from Λ (Huey et al. 1998). Observations which measure the growth of structure at intermediate red shifts ($z \sim 0.5 - 1.0$) are best suited for the purpose. In this red shift regime, structure growth is still occurring for the Λ model, but has shut off significantly for the Q model. The Ly-α determination of the mass power spectrum amplitude is at too high of a red shift to serve this purpose: at $z \sim 2.5$, evolution is still matter dominated for $\Omega_m = 0.3$ models with $w \lesssim -1/3$. Cluster abundances at $z \sim 0.5-1$ and the supernovae magnitude-red shift relation are better suited to this goal.

The shape of the mass power spectrum may prove to be a strong test of the QCDM scenario, if the observation of a turnover in the power spectrum near $k \sim 0.02-0.06$ h/Mpc and a break in the slope at higher wave numbers (Gaztanaga & Baugh 1998) bears out. It may prove difficult for the simplest, scalar field quintessence, or Λ for that matter, to generate such a feature. This is the subject of another investigation (Zlatev et al. 1999).

A test of the tracker quintessence scenario can be made by determining the change in the equation-of-state. If the equation-of-state can be measured at the present and at an earlier epoch, say $z \sim 1$, we can obtain a crude measure of the slope, dw/dt. Trackers have the special property that the equation-of-state becomes more negative at late times: $w \to -1$ as $\Omega_Q \to 1$. A measurement of $dw/dt > 0$ would argue against tracker quintessence.

More exotic observational tests can be used to discover the presence of a quintessence field. For example, if the quintessence field is coupled to the pseudoscalar $F_{\mu\nu}\tilde{F}^{\mu\nu}$ of electromagnetism as suggested by some effective field theory considerations (Carroll 1998), the polarization vector of a propagating photon will rotate by an angle $\Delta\alpha$ that is proportional to the change of the field value ΔQ along the path. CMB polarization maps can potentially measure the $\Delta\alpha$ from red shift ~ 1100 to now (Lue et al. 1999) and distant radio galaxies and quasars can provide information of $\Delta\alpha$ from red shift a few to now (Carroll 1998). If these two observations generate non-zero results, they can provide unique tests for quintessence and the tracker hypothesis, because tracker fields start rolling early (say, before matter-radiation equality) whereas most non-tracking quintessence fields start rolling just recently (at red shift of a few).

5. CONCLUSIONS

We have applied a battery of tests and constraints to the family of quintessence cosmological models, determining the range of parameters which are concordant with observations. The most reliable constraints are those resulting from low red shift observations, and the COBE normalization of the mass power spectrum. These restrict QCDM models to a narrow range of parameters, characterized by low matter density, $0.2 \leq \Omega_m \leq 0.5$, and negative equation-of-state, $-1 \leq w \lesssim -0.2$. While the intermediate red shift results are still developing, the implications are very exciting. The SNe observations narrow the range of matter density near $\Omega_m \sim 0.3-0.4$, and force the equation-of-state to $w \lesssim -0.4$. While this appears consistent with the core of the low red shift concordance, the potential for conflict is present if the matter power spectrum shape test demands $w \gtrsim -1$. Our results based on low red shift observations are given by Figures 6, 7; adding the supernovae constraints, which are more recent and whose systematic errors have not been fully tested, produces the narrower range shown in Figure 13.

To what degree do current uncertainties in the Hubble parameter, the spectral tilt and other cosmic parameters obstruct the resolution in w? To judge this issue, we have performed an exercise in which we fix $h = 0.65$, $\Omega_b h^2 = 0.019$, and we choose the spectral tilt to insure that the central values of the COBE normalization and the cluster abundance constraint are precisely satisfied. In Figures 14 and 15, we show how different constraints restrict the parameter planes. Note first the long, white concordance region that remains in the $\Omega_m - w$ plane, which is only modestly shrunken compared to the concordance region obtained when current observational errors are included. The region encompasses both Λ and a substantial range of quintessence. Hence, current uncertainties in other parameters are not critical to the uncertainty in w. The figure further shows how each individual constraint acts to rule out regions of the plane. The color or numbers in each patch represent the number of constraints violated by models in that patch. It is clear that regions far from the concordance region are ruled out by many constraints. Both figures also show that the boundaries due to the constraints tend to run parallel to the boundary of the concordance region. Hence, shifts in the values or the uncertainties in these measurements are unlikely to resolve the uncertainty in w by ruling out one side or the other — either the constraints will remain as they are, in which case the entire concordance region is allowed, or the constraints will shift to rule out the entire region.

New measurements not represented in this figure will be needed to distinguish Λ from quintessence. At this point, high precision measurements of the cosmic microwave background anisotropy are the most promising.

The results presented in this paper apply to quintessence models in which the equation-of-state is constant or slowly varying with time. In the latter case, setting $w = \widetilde{w}$, given in equation (3), gives an excellent approximation to the observational predictions for a broad class of models.

Particularly important classes of quintessence models are tracker and creeper fields. The tracker models are highly appealing theoretically because they avoid the ultra-fine tuning of initial conditions required by models with a cosmological constant or other (non-tracking) quintessence models. An additional important feature of these models is that they predict a definite relationship between the present day energy density and pressure, which yields a lower bound on the constant, effective equation-of-state, near $\widetilde{w} \sim -0.8$ (Steinhardt et al. 1999). Note that the effective or averaged equation-of-state as computed from Eq. (3) is about 10 per cent larger than the value of w today (given in Table I). In Figure 16 we add this bound to the low red shift constraints, obtaining the concordance region for tracker quintessence. This region retains the core of our earlier low red shift concordance, and is consistent with the SNe constraints. Creeper fields occur for the same potentials as trackers, but the initial energy density exceeds the radiation density at early times. The consequence is that the field rapidly rolls down the potential, towards a point which is only mildly (logarithmically) sensitive to the initial conditions, where it sticks and is effectively frozen with constant potential energy at very early times. Hence, the creeper field has an equation-of-state $w = -1$, and is effectively indistinguishable from a cosmological constant today.

In Figure 17 we combine all current observations on tracker models. Since these are arguably the best-motivated theoretically, we identify from this restricted region a sampling of representative models, listed in Table I, with the most attractive region for quintessence models being $\Omega_m \approx 0.33 \pm 0.05$, effective equation-of-state $w \approx -0.65 \pm 0.07$ and $h = 0.65 \pm 0.10$ and are consistent with spectral index $n_s = 1$ indicated by the dark shaded region in Figure 17. These models represent the best targets for future analysis. The challenge is to prove or disprove the efficacy of these models and, if proven, to discriminate among them.

We wish to thank Neta Bahcall, John Peacock and Michael Strauss for useful discussions. This research was supported by the US Department of Energy grants DE-FG02-92ER40699 (Columbia) and DE-FG02-91ER40671 (Princeton).

APPENDIX

Throughout this paper, we have chosen to judge models by combining observational constraints according to the "concordance" method in addition to the maximum likelihood estimator (MLE) method. We have asserted that the concordance method is conservative, sometimes giving a more reliable judge of the situation than the MLE method, especially when the observational constraints may be dominated by systematic, nongaussian, and/or correlated errors. We advocate using both concordance and MLE methods, as we have done in this paper, and then analyzing the source of any discrepancy before determining which models should be ruled out. Since it has been commonplace to present MLE results alone, we thought it would be useful to illustrate some of the pitfalls that can arise.

For this purpose, we employ a toy example in which we have two parameters, A and B, and two independent (observational) constraints, represented as the 2σ regions C_1 and C_2, which restrict the allowed ranges of parameters. This is meant to be a simplification of our real situation where we have a five-dimensional parameter space to analyze quintessence models, and we have many observational constraints. In our paper, we have tried to determine constraints in the Ω_m-w plane by projecting, effectively, from five-dimensions to two. In our toy model, we imagine projecting onto the A-axis to determine the constraint on A, indicated as a bar along the axis. Our interest is to compare the concordance region corresponding to 2σ with the 95%CL contour from the MLE method.

We present several simple examples in which there is a large disparity between the concordance and MLE procedures. In Figures 19, 18, we represent a two dimensional parameter space, A-B, with two independent constraint regions, $C_{1,2}$ shown as shaded rectangles. The projection of the concordance and MLE regions, C_{conc} and C_{MLE} respectively, onto the horizontal axis are shown as thick strips. Although the following discussion is qualitative, the relative sizes of the projected strips are correct.

Given the two observations, C_1 and C_2, the concordance region for A is obtained by: (a) finding their intersection in two-dimensions; and (b) projecting the two-dimensional intersection C_{conc} onto the A-axis to obtain a bar. Note that we do not project first, and then take the intersection. This method can lead to gross errors. For example, consider Figure

19, in which the C_1 and C_2 have no intersection at all. By our method, the concordance region is properly identified as the null set, whereas projecting first and then finding the intersection would produce a considerable band of acceptance, a false conclusion.

According to the MLE method, we are required to know the central value, $\vec{\mu}$, of each region, and assume the errors, $\vec{\sigma}$, are Gaussian. In the following, we make the simplistic assumptions that the likelihood function for each observation is symmetric about the center of the constraint region, C_1 or C_2. We weight each point $\vec{x}$ by a Gaussian $f(\vec{x},\vec{\mu},\vec{\sigma})$ for each of the two constraints, and identify C_{MLE}, the contour of constant $f_1 f_2$ or χ^2 which contains 95% of the total probability, $\int_C f_1 f_2 d\vec{x} = 0.95 \int f_1 f_2 d\vec{x}$. This is a straightforward procedure.

Case 1: Figure 18 illustrates a case where C_1 encompasses C_2. In this situation, the MLE method (indicated by the lower bar) produces a *smaller* acceptance region than the concordance method. If the errors are truly gaussian and uncorrelated, the conclusion based on MLE is the better representation of uncertainty. Note that the concordance region includes the MLE region plus an additional range of A; so, the error made with concordance is to include too much. However, no model is ruled out by concordance which intuition suggests ought not be eliminated. We call this "conservative," and our aim is to find a robust, conservative method.

The MLE is not a robust, conservative method, as can be illustrated by the same figure. Suppose that the observations in C_1 and C_2 are suspected to be nongaussian or systematic or correlated. Then, we are clearly mistaken to rely on the MLE method and eliminate the range of A which lies within the concordance region but outside the MLE region. In this example, the difference is only modest, but if we were combining a number of observations, the MLE allowed region would be much tinier than the concordance region, and the error in trusting the MLE method would be more serious. This point is directly relevant to this paper.

Case 2: The observational constraints C_1 and C_2 intersect in a small region or, as illustrated in Figure 19, have no intersection at all. This case is opposite to Case 1 in that the MLE method produces a *larger* acceptance region than the concordance method. For example, the concordance region in Figure 19 is the null set, whereas the MLE contour suggests a large acceptance region. This is not a case where the MLE method is being conservative; rather, it is a case where the MLE method is misleading. Intuition dictates that the observational constraints are in conflict, and the concordance method reflects this conclusion by producing a null concordance region. The MLE method, taken at face value, suggests a broad range of agreement. To be fair to the MLE methodology, one is not supposed to accept the 95% MLE contour at face value. The contour represents a probability compared to the maximum likelihood point, and one is supposed to check that this point is indeed a good fit. In practice, though, this step is often ignored or discounted. For example, if the maximum likelihood point has a high value of χ^2 by the conventional χ^2-test, this is often (properly) considered a problem due to underestimating experimental errors. But, as indicated by this example, the same statistical result can be an indication that there is a true contradiction between models and data, and that completely new models need to considered. Hence, a contradiction between concordance and MLE methods is a warning to examine closely the cause.

Case 3: Suppose constraint C_2 is obtained by combining many measurements with small statistical uncertainty but unknown correlated error. Then, in a MLE analysis, constraint C_2 receives undue statistical weight.

If we drop the simplistic assumption that the likelihood function for each individual constraint is symmetric about the center of the constraint region, which is rare, other kinds of discrepancies between concordance and maximum likelihood can occur. For example, the MLE region may be shifted with respect to the concordance region so that each test allows models which the other does not.

As a prominent example, the current, highly provocative measurements of type 1a supernovae by the High-Z Supernova Search Team (HZS: Riess et al. 1998, Garnavich et al. 1998) and the Supernova Cosmology Project (SCP: Perlmutter et al. 1998) exemplify all three cases above. For the HZS data based on MLCS (multi-color light curve shape) analysis or for SCP using the Fit C selected data set Perlmutter et al. 1998, the concordance region is significantly larger than the MLE acceptance region, as demonstrated by comparing Figures 10 and 13. So, relying on the MLE 95%CL region eliminates models which formally pass the absolute χ^2 test at the 95% level. While statisticians may argue that the MLE likelihood estimate is more reliable *assuming uniform prior* over the parameter space, in comparing qualitatively different models (which do not have uniform prior), the readers should beware that MLE can potentially rule out an entire model even if the model agrees at better than the 95% confidence level (as judged by χ^2). Especially at this early stage when better data will soon be available, we advocate the more cautious, concordance approach. This first example is like Case 1. We have also noted that the scatter in the supernova red shift - magnitude data is so wide that no model which we have tested passes a χ^2 test with the SCP full data set. Hence, this is an example, like Case 2, where the concordance region is null but the MLE acceptance region is large. Finally, in a MLE or Fisher matrix analysis which combines the supernovae measurements with other observations, the fact that there are many individual supernovae with small reported uncertainty gives these measurements heavy statistical weight. However, as the survey teams admit, the measurement approach is new and there remains the possibility that as yet unidentified physical effects cause a systematic, apparent reddening of the data. As in Case 3, results obtained by simple statistical combination of supernovae data with other measurements should be viewed cautiously.

Another feature of maximum likelihood analysis, well-known to practitioners but perhaps unappreciated by some, is the fact that the estimation of parameters in a multi-dimensional fit can be markedly different from the estimate when marginalizing over some parameters. For example, the range of w spanned by the MLE 95% confidence region in the Ω_m-w plane (as considered by Perlmutter et al. 1999 and in this paper) is significantly narrower than the MLE 95% confidence region in the three-dimensional parameter space including h and significantly broader than the MLE 95% confidence region obtained by marginalizing over Ω_m and collapsing to a one-parameter fit to w. (This is due to the fact that $\Delta\chi^2$ criterion for 95% confidence depends on the dimensionality of the parameter space.)

These simple cases demonstrate the differences in the concordance and MLE procedures and, especially, some problems which can arise in MLE analysis. Because we maintain the position that systematic uncertainties dominate the errors in constructing the constraint regions, we advocate the concordance approach as being more conservative for cosmological analysis at the present time. In general, caution must be exercised when the two methods disagree significantly, and the source of the discrepancy must be understood in order to determine the true acceptance region.

REFERENCES

Affleck, I. et al. 1985, Nucl Phys B, 256, 557
Bahcall, N. A. & Fan, X. 1998, ApJ, 504, 1
Bahcall, N. A., Fan, X., & Cen, R. 1997, ApJ, 485, L53
Banks, T. 1996, hep-th/9601151
Bardeen, J. 1986, in InnerSpace/OuterSpace, ed. Edward W. Kolb, Michael S. Turner, David Lindley, Keith Olive, & David Seckel (Chicago: University of Chicago Press), 212
Barreiro, T., Carlos, B. & Copeland, E. J. 1998, Phys. Rev. D, 57, 7354
Bartelmann, M. *et al.* 1998, Astron. Astrophys., 330, 1
Bennett, C. L., et al. 1996, ApJ, 464, L1
Bertschinger, E. & Dekel 1989, ApJ, 335, L5
Binetruy, P., Gaillard, M. K. & Wu, Y.-Y. 1996, Nucl Phys B, 481, 109
Binetruy, P. 1999, Phys. Rev. D, 60, 063502
Blanton, M., Cen, R. Ostriker, J. P., & Strauss, M. 1998, ApJ, 522, 590
Bond, J. R. 1995, Astrophys Lett & Comm, 32, 63
Bond, J. R., Jaffe, A. H., & Knox, L. 1998, astro-ph/9808264
Bunn, E. F. & White, M. 1997, ApJ, 480, 6
Burles, S. & Tytler, D. 1997, ApJ, 499,699
Burles, S. & Tytler, D. 1997, ApJ, 507, 732
Burles, S. & Tytler, D. 1998, SSRv, 84, 65B (astro-ph/9712265)
Caldwell, R. R., Dave, R., & Steinhardt, P. J. 1998, Phys. Rev. Lett., 80, 1582
Caldwell, R. R., & Steinhardt, P. J. 1998, Phys. Rev. D, 57, 6057
Carlberg, R. G., Morris, S. M., Yee, H. K. C., & Ellingson, E. 1997, ApJ, 479, L19
Carroll, S. 1998, Phys. Rev. Lett., 81, 3067.
Cen, R. & Ostriker, J. P. 1998, astro-ph/9809370
Chaboyer, B. *et al.* 1998, ApJ, 494, 96
Cheng, Y.-C. & Krauss, Lawrence M. 1999, ApJ, 514, 25.
Chiu, W., Ostriker, J.P. and Strauss, M.A. 1998, ApJ, 494, 479
Cheng, E. S. *et al.* 1997, ApJ, 488, L59
Coble, K. et al. 1997, Phys. Rev. D, 55, 1851
Croft, R. A. C. *et al.* 1998, ApJ, 495, 44
Croft, R. A. C. *et al.* 1998, ApJ, 520, 1
da Costa, L.N. *et al.* 1998, MNRAS, 299, 425
Dave, R. 1998, PhD. Thesis, University of Pennsylvania
Davis, M. *et al.* 1985, ApJ, 292, 371
Davis, M., Nusser, A., & Willick, J. 1993, ApJ, 473, 22
Dekel, A. *et al* 1999, ApJ, 522, 1
Devlin, M. J. *et al.* 1998, ApJ, 509, L69
Evrard, August E. 1997, MNRAS, 292, 289
Falco, E. E. *et al.* 1997, ApJ, 484, 70
Falco, E. E., Kochanek, C. S., & Munoz, J. A. 1998, ApJ, 494, 47
Ferreira, P. G. & Joyce, M. 1997, Phys. Rev. Lett., 79, 4740
Ferreira, P. G. & Joyce, M. 1998, Phys. Rev. D, 58, 023503
Freedman, W. L. *et al.* 1998, in IAU Symp. 183, Cosmological Parameters and the Evolution of the Universe, ed. K. Sato (astro-ph/9801080)
Freudling, W. *et al.* 1999, ApJ, 523, 1
Frieman, J. et al., 1995, Phys. Rev. Lett., 75, 2077
Fry, J. N. 1986, ApJ, 461, L65
Fukugita, M., Hogan, C. J., & Peebles, P. J. E. 1997, ApJ, 503, 518
Gardner, J. P., *et al.* 1997, ApJ, 486, 42
Garnavich, P. M. *et al.* 1998, ApJ, 509, 74
Gaztanaga, E., & Frieman, J. A. 1994, ApJ, 437, L13
Gaztanaga, E. & Baugh, C. M. 1998, MNRAS, 294, 229
Giovanelli *et al*, 1998, ApJ, 505, L91
Gorski, K. M. *et al.* 1996, ApJ, 464, L11
Gorski, K. M. *et al.* 1998, ApJ, 114, 1
Gott, J. R., III 1982, Nature 295, 304
Hamuy, M. *et al.* 1996, AJ, 112, 2398
Hancock, S. *et al.* 1998, MNRAS, 294, L1
Herbig, T. *et al.* 1998, ApJ, 509, L73
Hill, C. & Ross, G. G. 1988, Nuc Phys B, 311, 253
Hill, C. & Ross, G. G. 1988, Phys Lett B, 203, 125
Hinshaw, G. *et al.* 1996, ApJ, 464, L25
Hu, W. 1999, ApJ, 506, 485
Hudson, M.J. *et al.* 1999, ApJ, 512, L79
Huey, G., Wang, L., Dave, R., Caldwell, R. R., & Steinhardt, P. J. 1999, Phys. Rev. D, 59, 063005
Huey, G. & Steinhardt, P. J. 1999, in preparation.
Hui, L. 1999, ApJ, 516, 519
Hui, L., Stebbins, A. & Burles, S. 1999, ApJ, 511, 5
Jenkins, E., *et al.* 1999, ApJ, 520, 182
Kaiser, N. 1986, in InnerSpace/OuterSpace, ed. Edward W. Kolb, Michael S. Turner, David Lindley, Keith Olive, & David Seckel (Chicago: University of Chicago Press), 258
Keeton, C. R. & Kochanek, C. S. 1997, ApJ, 487, 42
Kochanek, C. S. 1995, ApJ, 453, 545
Kochanek, C. S. 1996, ApJ, 466, 638
Krauss, L.M. & Turner, M.S., Gen Rel Grav 27, 1137
Kundic, T. *et al.* 1997, AJ, 114, 507
Lauer, T. & Postman, M. 1994, ApJ, 425, 418
Lauer, T. *et al.* 1998, ApJ, 499, 577
Leitch, E. M. *et al.* 1998, astro-ph/9807312
Levshakov, S. 1998, astro-ph/9808295
Linde, A. 1999, Phys. Rev. D, 59, 023503
Lubin, L. *et al.* 1996, ApJ, 460, 10
Lue, A., Wang, L. & Kamionkowski, M. 1999, Phys. Rev. Lett., 83, 1506
Malhotra, S., Rhoads, J. & Turner, E. 1997, MNRAS, 288, 138
Maoz, D. *et al* 1993, ApJ, 409, 28
Maoz, D. & Rix, H.-W. 1993, ApJ, 416, 425
Mauskopf, P.D., et al. 1999, astro-ph/9911444.
McDonald, P. & Miralda-Escude, J. 1998, ApJ, 518, 24
McGaugh, S. 1998, ApJ, 499, 41
Miller, A.D., et al. 1999, ApJ, 524, L1.
Mo, H. J. & Fukugita, M. 1996, ApJ, 467, L9
Myers, S. T. *et al.* 1997, ApJ, 492, 110
Netterfield, B. *et al.* 1997, ApJ, 474, 47
Olive, K., Steigman, G. & Walker, T. 1999, astro-ph/9905320
Oliveira-Costa, A. *et al.* 1998, ApJ, 509, L77
Ostriker, J. P. & Steinhardt, P. J. 1995, Nature 377, 600
Paczynski, B., private communication
Peacock, J. 1997a, MNRAS, 284, 885
Peacock, J. 1997b, private communication
Peebles, P. J. E. & Ratra, B. 1988, ApJ, 325, L17
Perlmutter, S. *et al* 1998, ApJ, 517, 565
Perlmutter, S., Turner, M. S., and White, M., Phys. Rev. Lett., 83, 670
Platt, S. R. *et al.* 1997, ApJ, 475, L1
Press, W. H. & Schechter, P. 1974, ApJ187, 425
Ratra, B. & Peebles, P. J. E. 1988, Phys. Rev. D, 37, 3406
Ratra, B. & Quillen, A. 1992, MNRAS, 259, 738
Riess, Adam G. *et al.* 1998, AJ, 116, 109
Salaris, M. & Weiss, A. 1998, Astron. Astrophys., 335, 943
Schechter, P. L. *et al.* 1997, ApJ, 475, L85
Schramm, D. N. & Turner, M. S. 1998, Rev Mod Phys, 70, 303
Scott, P. F. *et al.* 1996, ApJ, 461, L1
Sigad, Y. *et al.* 1998, ApJ, 495, 516
Silveira, V. & Waga, I. 1997, Phys. Rev. D, 56, 4625
Seljak, U. & Zaldarriaga 1996, ApJ, 469, 437
Spergel, D. & Pen, U.-L. 1996, ApJ, 491, L67
Steidel, C. C. *et al.* 1998, ApJ, 492, 428
Steinhardt, P. J., Wang, L., & Zlatev, I. 1999, Phys. Rev. D, 59, 123504
Strauss, Michael 1997, in Critical Dialogues in Cosmology, ed. Neil Turok (Singapore: World Scientific), 423
Tammann, G. A. 1998, in Proceedings of the 8th Marcel Grossman Syposium, ed. T. Piran (Singapore: World Scientific) (astro-ph/9805013)
Tegmark, M & Peebles, P. J. E. 1998, ApJ, 500, L79
Bloomfield-Torres, L. F. & Waga, I. 1996, MNRAS, 279, 712
Turner, E. L., Ostriker, J. P. & Gott, J. R. III 1984, ApJ, 284, 1
Turner, M. S. & White, M. 1997, Phys. Rev. D, 56, R4439
Waga, I. & Miceli, A. P. M. R. 1999, Phys. Rev. D, 59, 1035
Wambsganss, J., Cen, R., & Ostriker, J. P. 1998, ApJ, 494, 29
Wang, L. & Steinhardt, P. J. 1998, ApJ, 508, 483
Weinberg, D. H. *et al.* 1998, ApJ, 522, 563
Weiss, N. 1987, Phys. Rev. Lett., 197, 42
Wetterich, C. 1995, Astron. Astrophys., 301, 321
White, S. D. M. *et al.* 1993, Nature, 366, 429
Willick, J. *et al.* 1997, ApJ, 486, 629
Willick, J. & Strauss, M. 1998, ApJ, 507, 64
Wu, X.-P. & Mao, S. 1996, ApJ, 463, 404

Zaroubi, S. *et al.* 1997, ApJ, 486, 21
Zehavi, I. 1998, PhD Thesis, Hebrew University
Zlatev, I., Wang, L., & Steinhardt, P. J. 1998, Phys. Rev. Lett., 82, 896
Zlatev, I., Wang, L., Caldwell, R. R., & Steinhardt, P. J. 1999, in preparation

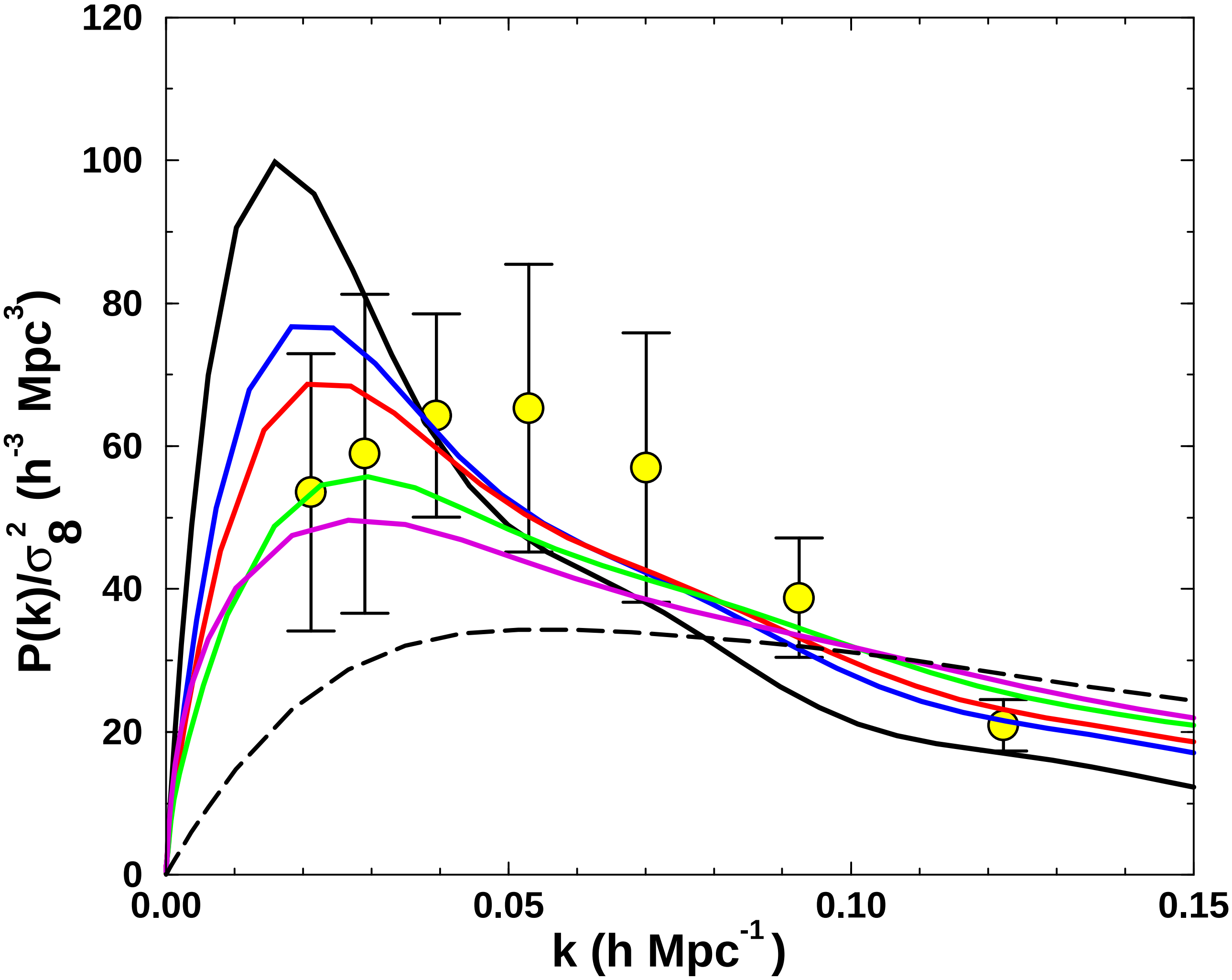

FIG. 1.— The solid circles with 1σ error bars are the Peacock APM data we use to test the power spectra shape. The five solid lines are quintessence models that pass the shape test with a confidence level of 95%. The model parameters for the black, blue, red, green, and purple curves are: $w =$ -1, -1/2, -1/3, -1/6, 0; $\Omega_Q = 0.70, 0.60, 0.55, 0.43, 0.20$; $\Gamma = 0.20, 0.26, 0.29, 0.37, 0.52$. The bias factor is optimized for each model shown in order to obtain the minimum χ^2: $b = 1.01, 1.24, 1.46, 1.81, 2.49$, respectively. All models have $n_s = 1$ and $\Omega_b h^2 = 0.02$. For comparison, the dashed line is a standard CDM model with best-fit bias 0.8 which fails the shape test.

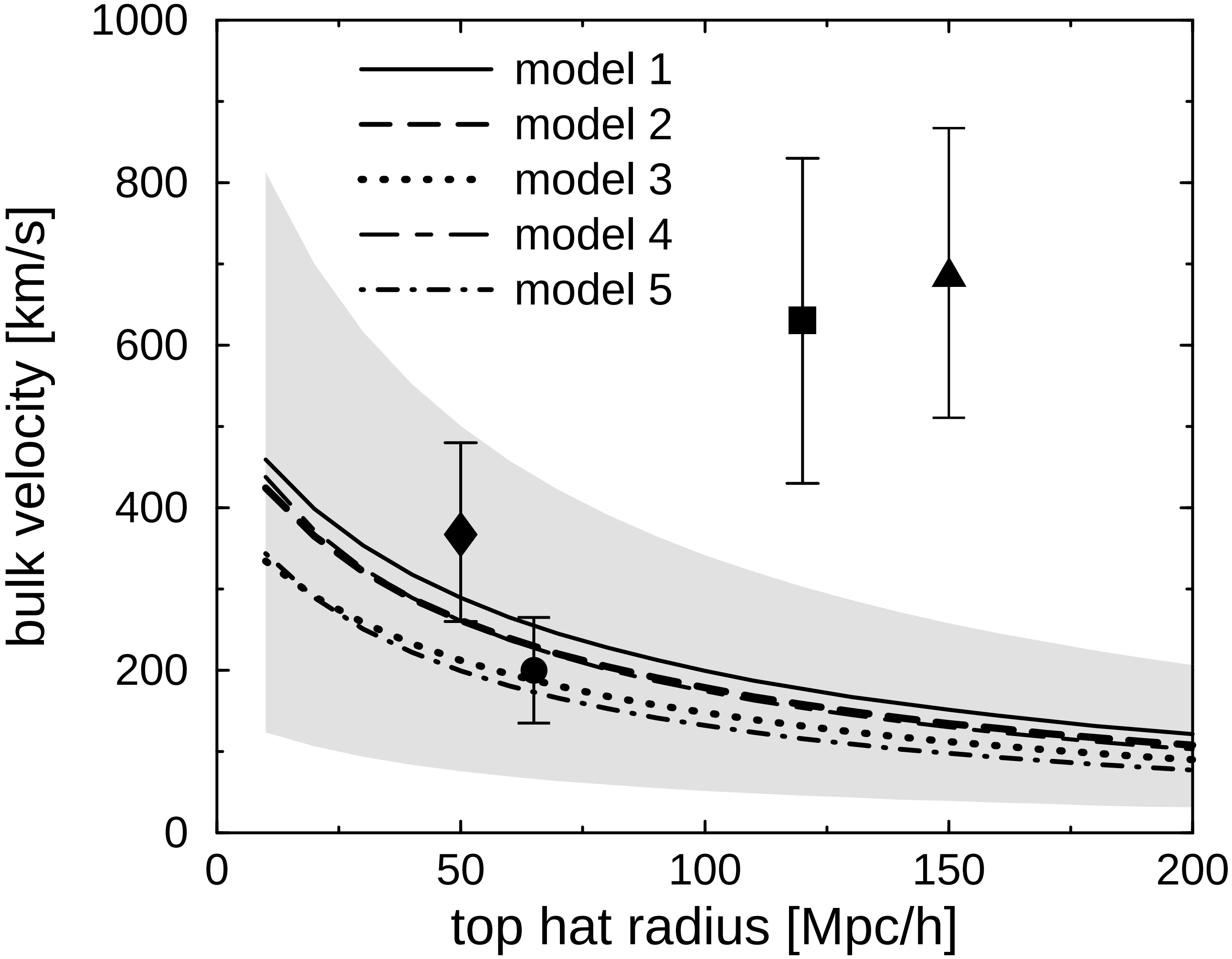

FIG. 2.— The bulk velocity predictions as a function of radius (assuming a top hat window function) are shown for a representative set of QCDM models, and ΛCDM given at the end of this paper in Table I. Surrounding the best-fit quintessence model (Model 2), we have shown the shaded sheath corresponding to the 95%CL, according to a Maxwellian distribution of bulk velocities. The diamond, circle, square, and triangle show the bulk velocities measured by Dekel et al. 1999, Giovanelli et al. 1998, Hudson et al. 1999, Lauer & Postman 1994 with 2σ error bars, respectively. We have idealized the window function for the galaxy velocity catalog, assuming a spherical top hat.

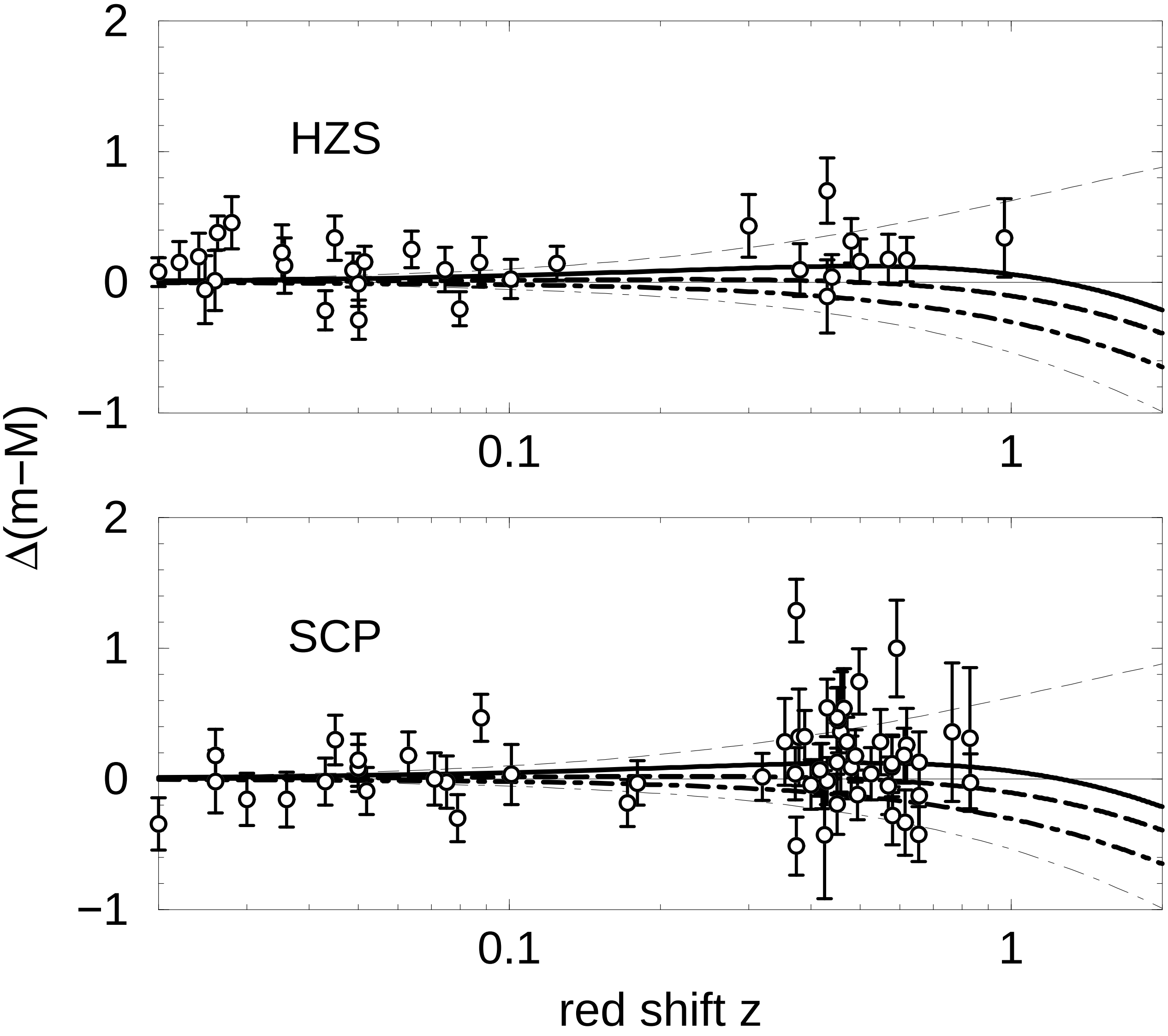

FIG. 3.— The magnitude - red shift relationship determined by type 1a SNe is shown, for the HZS (using the MLCS analysis method) above, and SCP (full data set) below. The horizontal $\Delta(m-M)=0$ reference line shows the prediction of an empty universe ($\Omega_{total}=0$), which has been subtracted from all data and theoretical curves. The thin dashed and dot-dashed curves show the predicted magnitude-red shift relationship for flat models with $\Omega_\Lambda=1$ and $\Omega_m=1$, respectively. The vertical offset of the data has been determined by minimizing the χ^2 to the best fit ΛCDM model with $\Omega_m=0.3$, which is given by the thick, solid curve. The predictions for quintessence (QCDM) models with $w=-2/3$, $-1/3$ for the same matter density are shown by the thick dashed and dot-dashed curves.

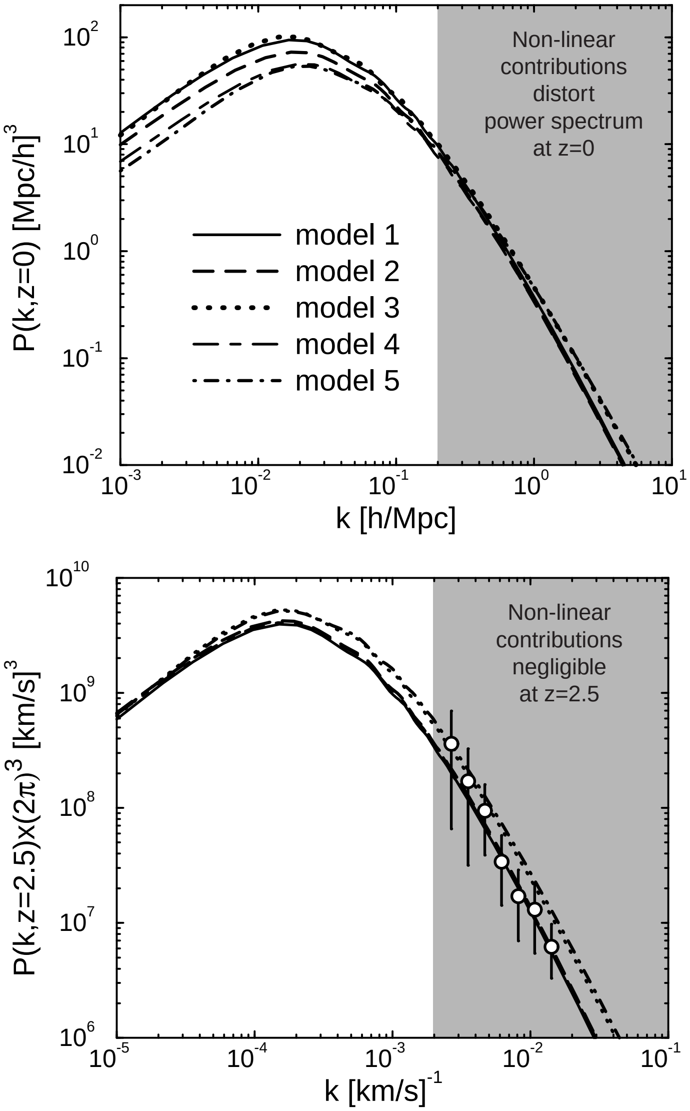

FIG. 4.— The upper panel compares the linear mass power spectrum at $z = 0$ for the representative ΛCDM and QCDM models in Table I. All models are COBE normalized and satisfy the cluster abundance constraint on σ_8. The solid and dashed curves have $n_s = 1$; the dotted and dot-dashed curves have $n_s = 1.2$. The shaded region in the top panel indicates where non-linear contributions are non-negligible. The lower panel shows the same power spectra projected back in time to red shift $z = 2.5$ and rescaled by the appropriate value of h at red shift z. Note that, in converting to $z = 2.5$, the abscissa in the lower panel has been rescaled so that it is expressed in terms of velocity; once this model-dependent rescaling is made, the models can be compared directly to the data. We show the constraints on the power spectrum, with 1σ error bars, as deduced from the Ly-α forest. Among our representative models, the $n_s = 1$ models are preferred over the $n_s = 1.2$ models.

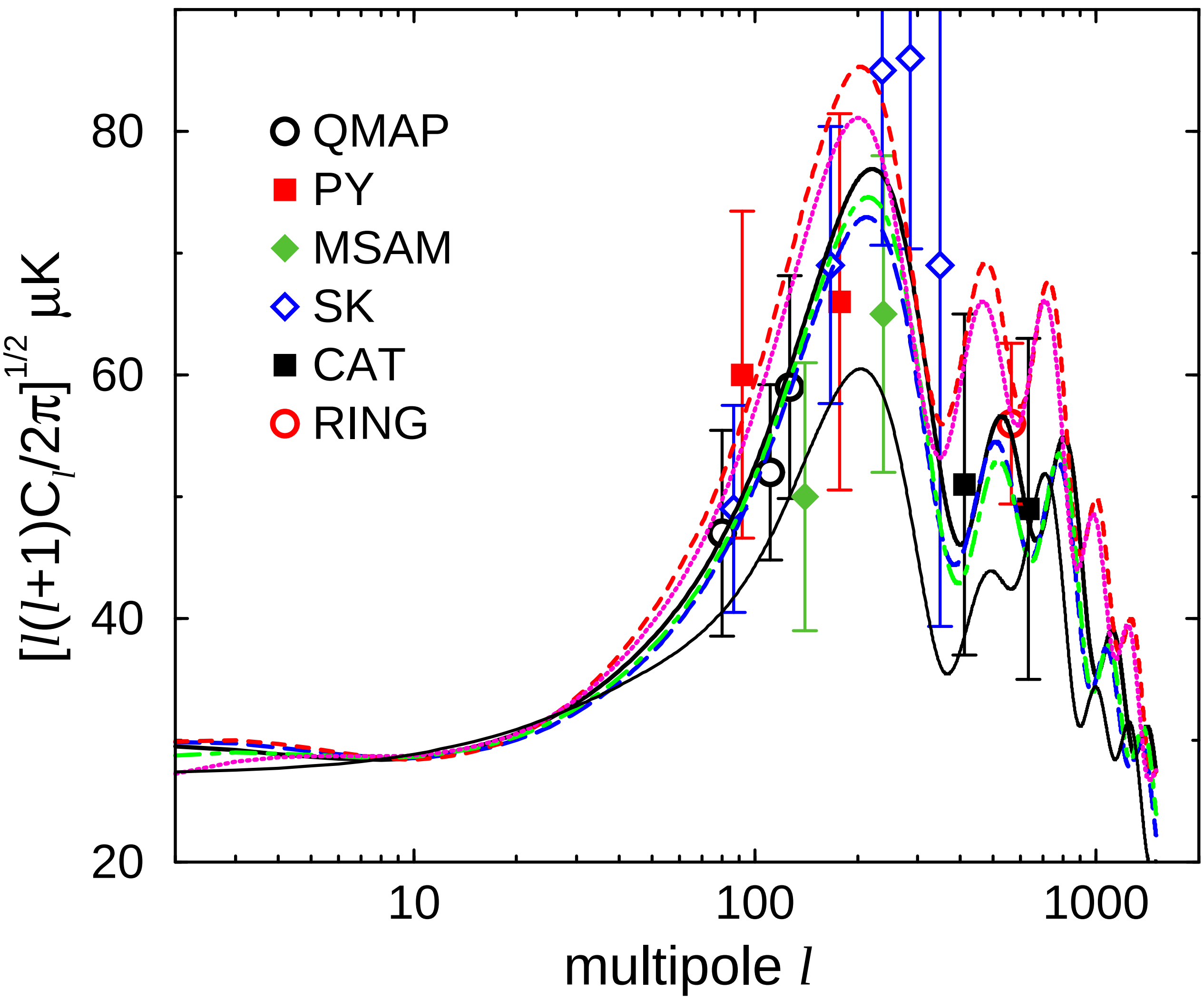

Fig. 5.— The bandpower averages used as the basis of the small angle CMB constraint are shown. For comparison, the black, blue, red, green, and purple curves are models 1-5, given at the end of this paper in Table I. The differences are small, but distinguishable in near-future experiments. All have acoustic peaks lying significantly above those of the standard cold dark matter model (thin black). The higher ℓ results favor our representative models with $n_s = 1$ over those with $n_s = 1.2$.

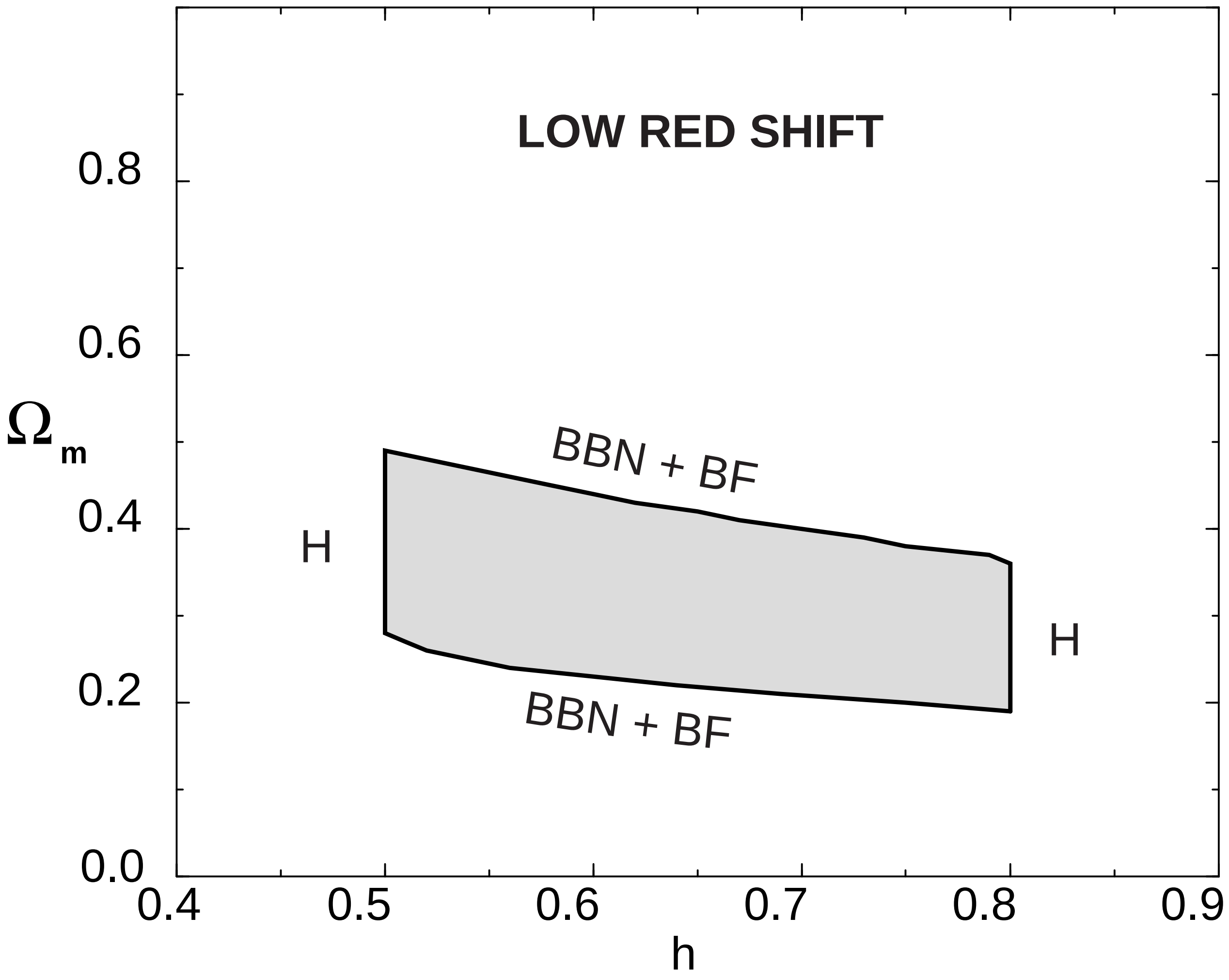

Fig. 6.— The projection of the concordance region on the $\Omega_m - h$ plane, on the basis of the low red shift observational constraints only, is shown. The observations which dominate the location of the boundary are labeled.

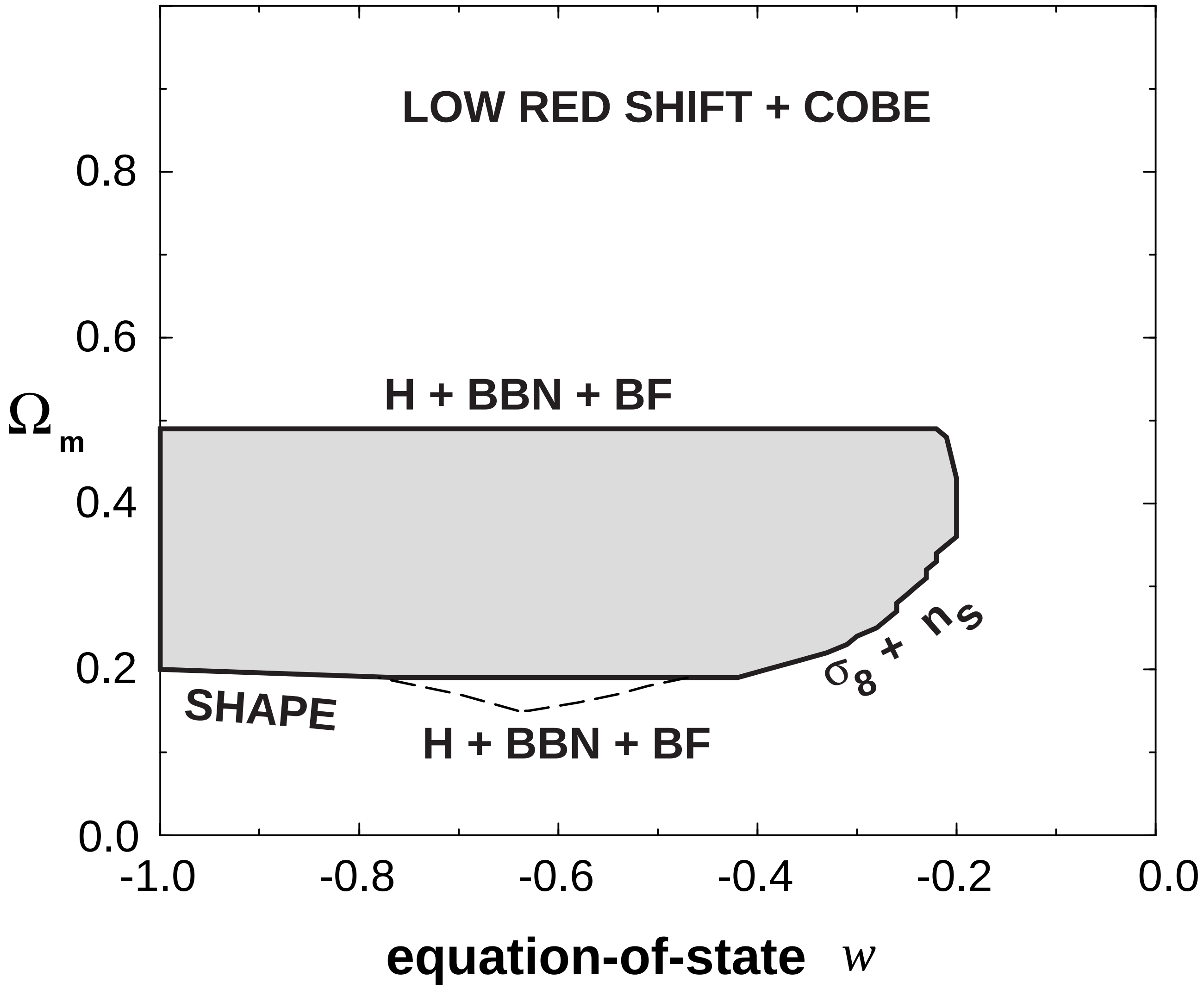

FIG. 7.— The projection of the concordance region on the $\Omega_m - w$ plane, on the basis of the low red shift and COBE observational constraints only, is shown. The observations which dominate the location of the boundary are labelled. If a wider range for the baryon density is allowed, such as $0.006 < \Omega_b h^2 < 0.022$, the shape test and σ_8 constraint determine the location of the low Ω_m boundary, and the concordance region extends slightly as shown by the light dashed line.

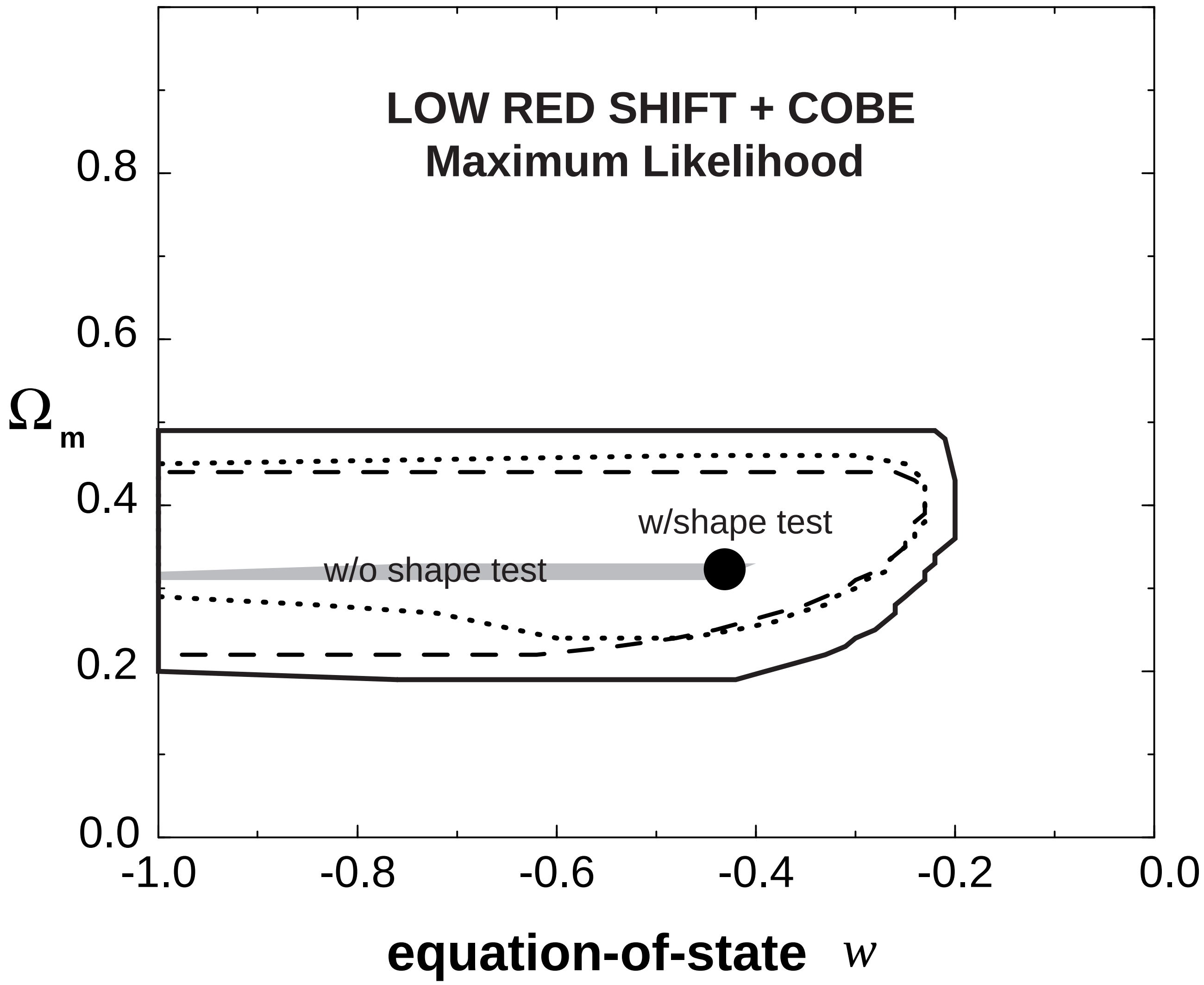

FIG. 8.— The 2σ maximum likelihood contours in the $\Omega_m - w$ plane with the low red shift and COBE observational constraints only are shown. The dotted and dashed curves show the likelihood contours with and without the mass power spectrum shape test. The set of models which maximize the likelihood in each case are shown by the solid circle and the thick line. The shape test pushes models away from $w = -1$, towards $w \sim -1/2$. The solid line shows the 2σ allowed region according to the concordance region for comparison.

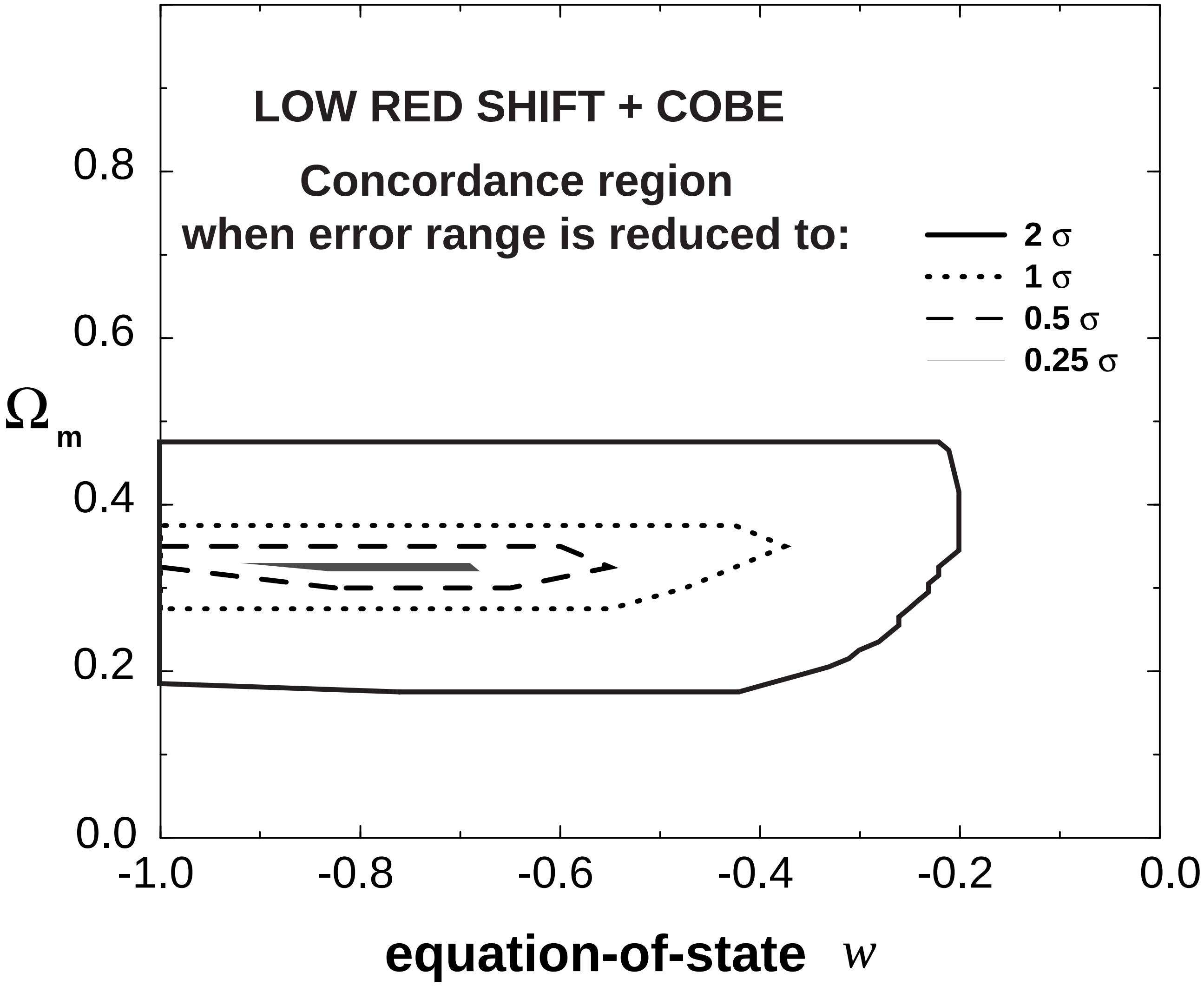

FIG. 9.— We carry out the exercise of shrinking the error bars on all measurements to obtain the equivalent 'best fit' models in the concordance approach. The surviving models have $\Omega_m \sim 0.33$ and $-0.9 < w < -0.7$. This is similar to the best fit models obtained from the maximum likelihood method, however the concordance models are not as strongly affected by the shape test.

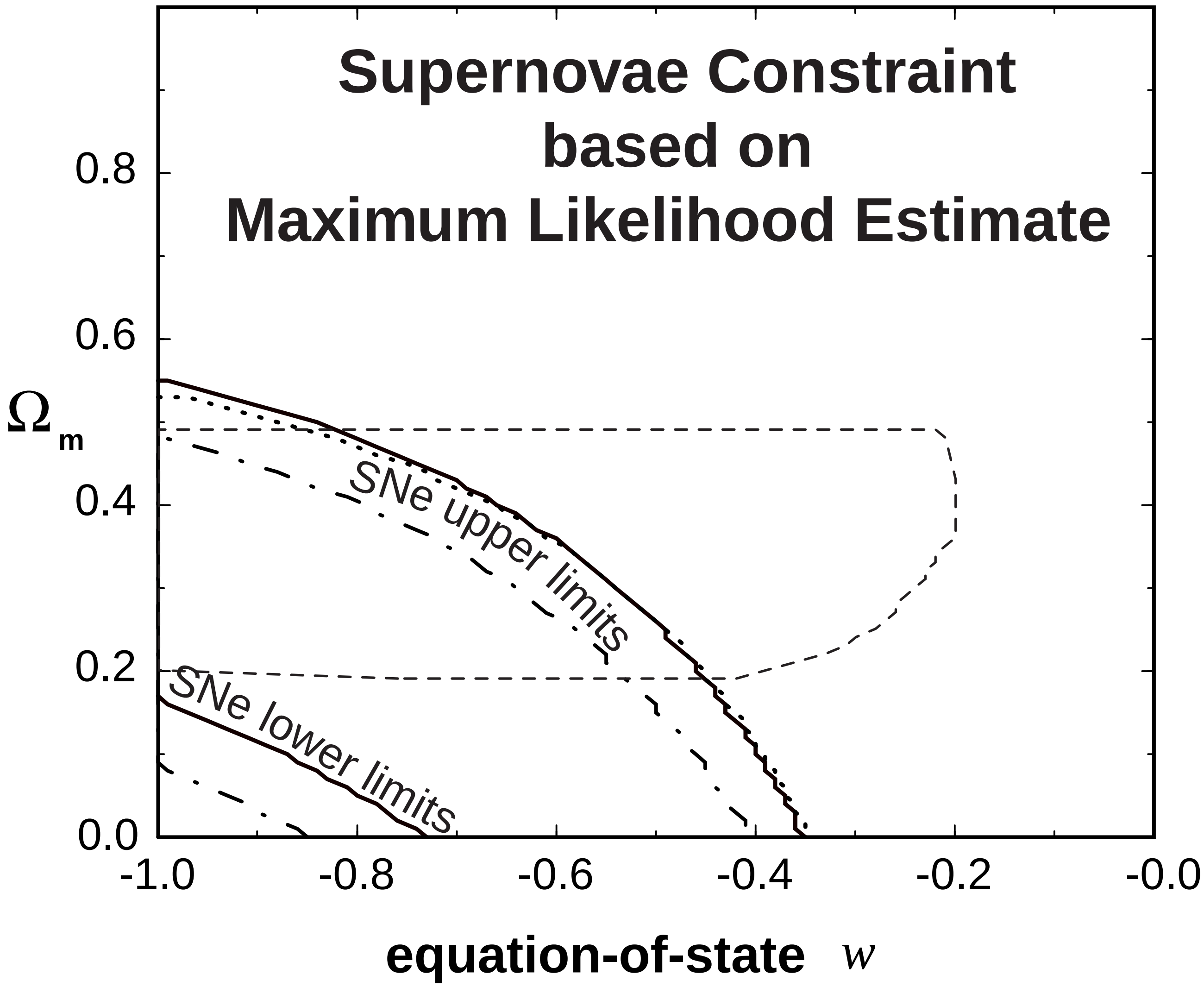

FIG. 10.— The 2σ maximum likelihood constraints on the $\Omega_m - w$ plane, due to the SCP (solid), HZS MLCS (short dashed), and HZS template fitting methods (dot-dashed). The light, dashed line shows the low red shift concordance region.

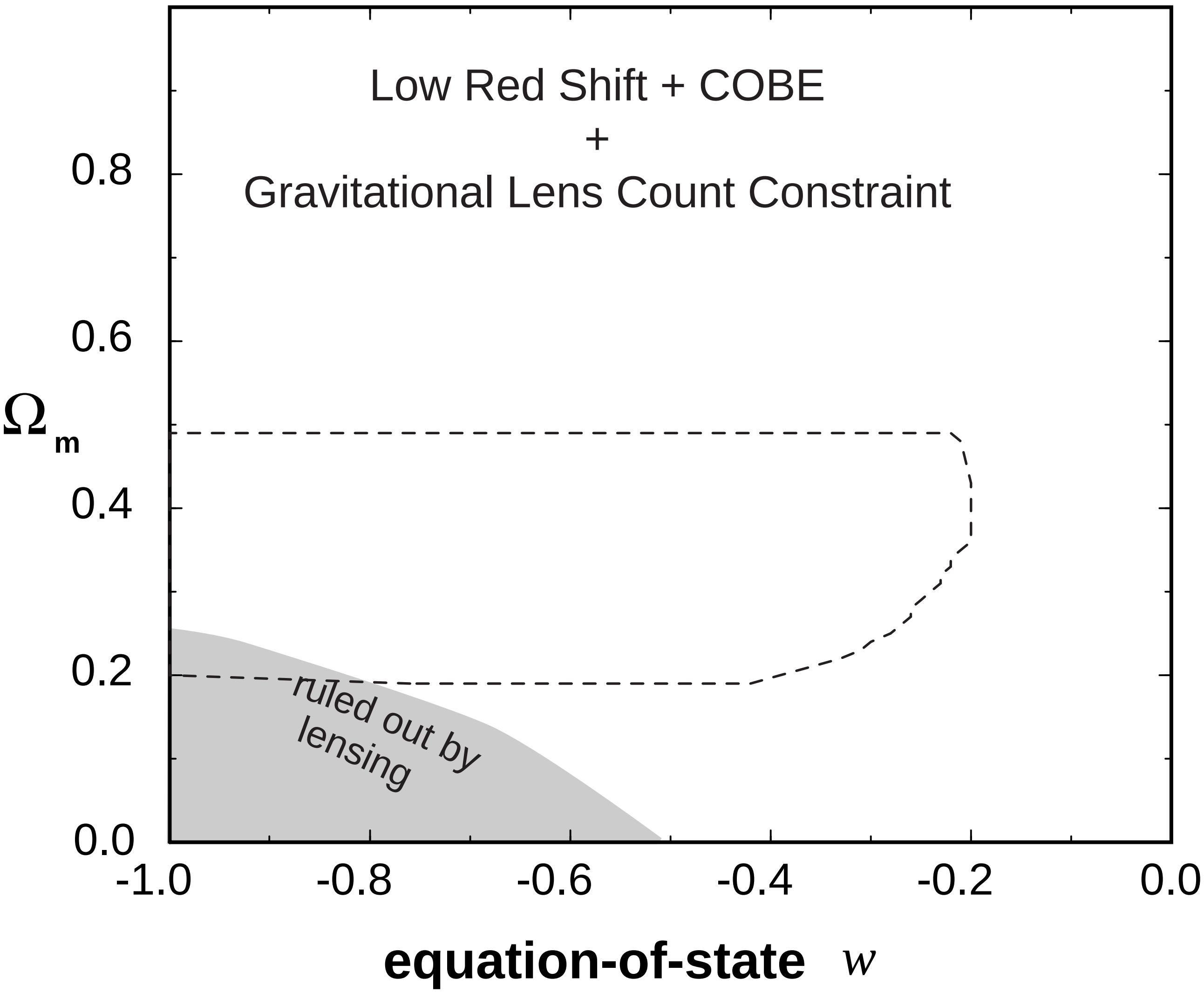

FIG. 11.— The 2σ gravitational lensing constraint on the low red shift concordance region is shown.

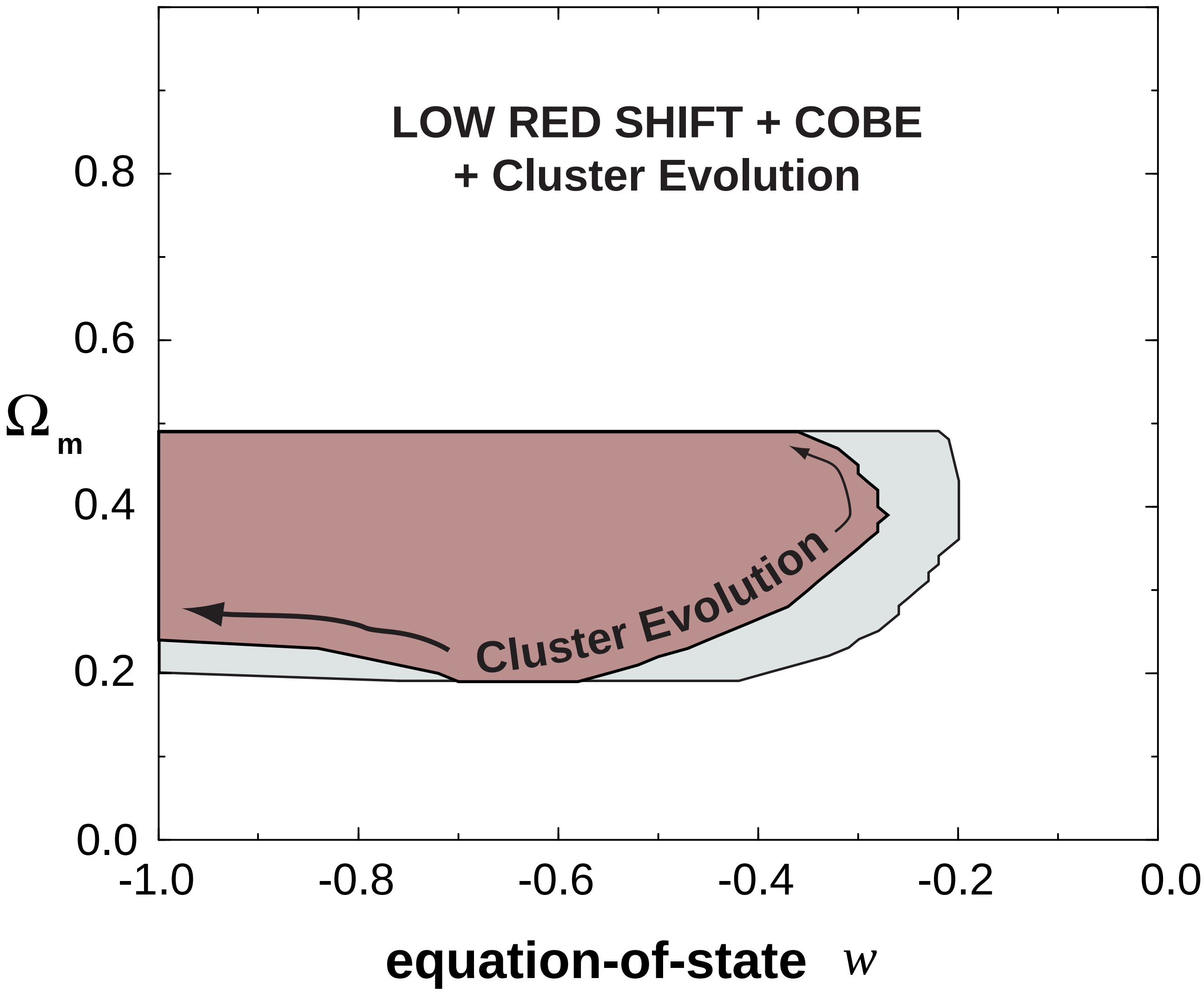

FIG. 12.— The effect of the x-ray cluster abundance evolution constraint on the projection of the concordance region to the $\Omega_m - w$ plane is shown by the dark shaded region. The light shaded region is due to the low red shift constraints only.

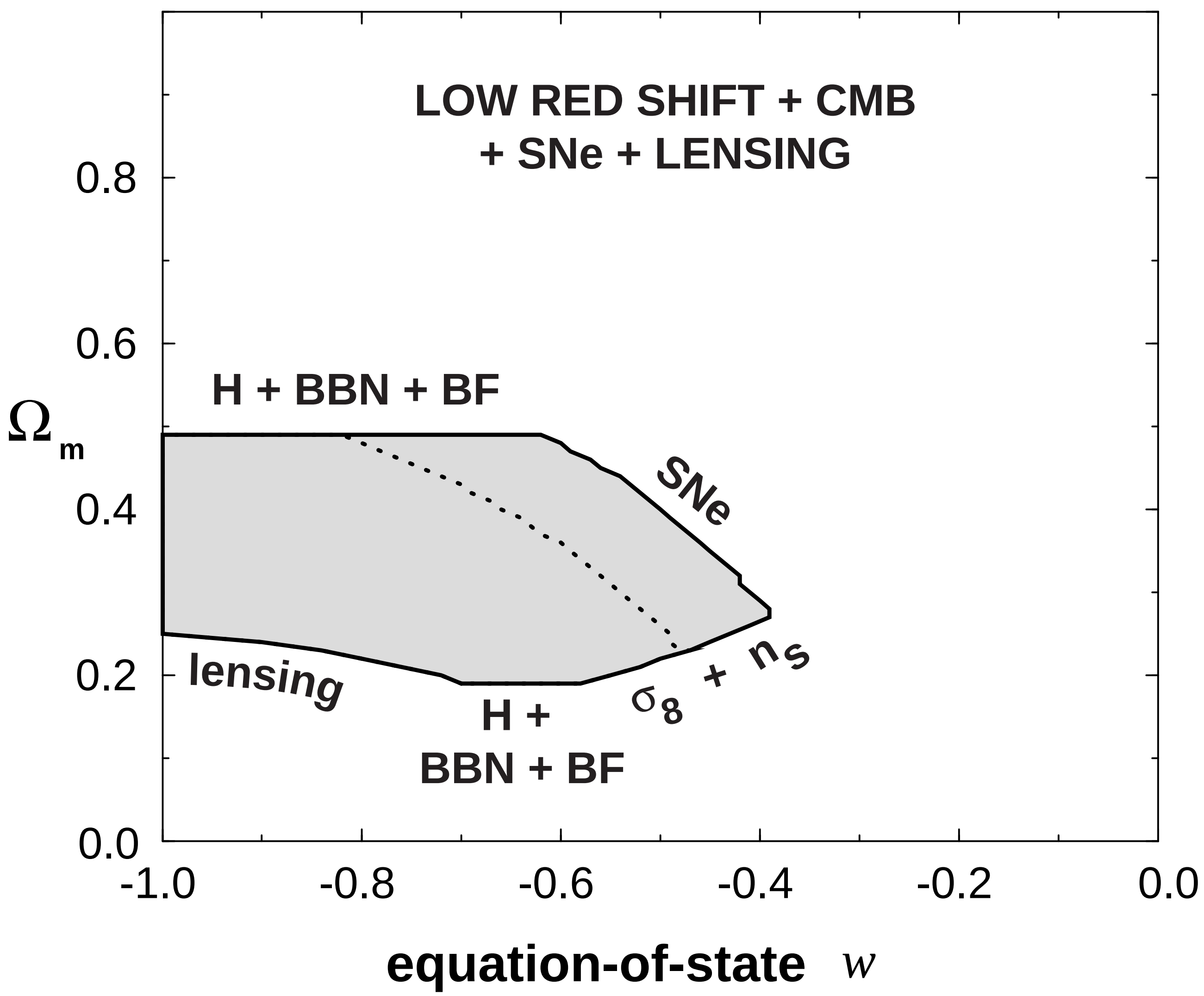

FIG. 13.— The dark shaded region is the projection of the concordance region on the $\Omega_m - w$ plane with the low, intermediate, and high red shift observational constraints. The dashed curve shows the 2σ boundary as evaluated using maximum likelihood, which is the same as Figure 10 (See the Appendix for a comparison of the tests and a discussion of the pitfalls of the maximum likelihood approach.)

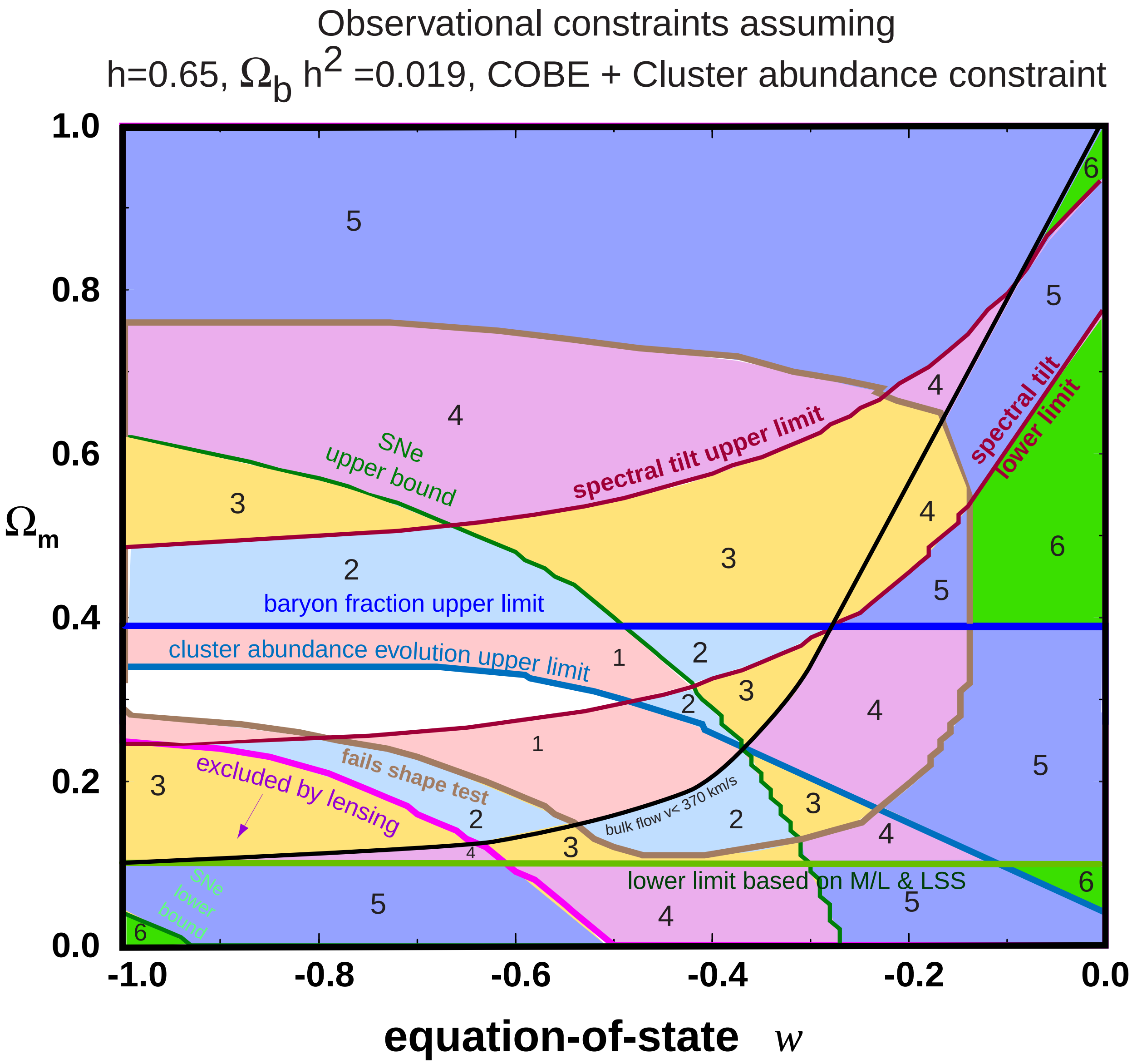

FIG. 14.— The concordance region (white) resulting if we artificially set $h = 0.65$ and $\Omega_b h^2 = 0.019$ precisely and fix the spectral tilt to precisely match the central values of COBE normalization and cluster abundance measurements. The curves represent the constraints imposed by individual measurements. The curves divide the plane into patches which have been numbered (and colored) according to the number of constraints violated by models in that patch.

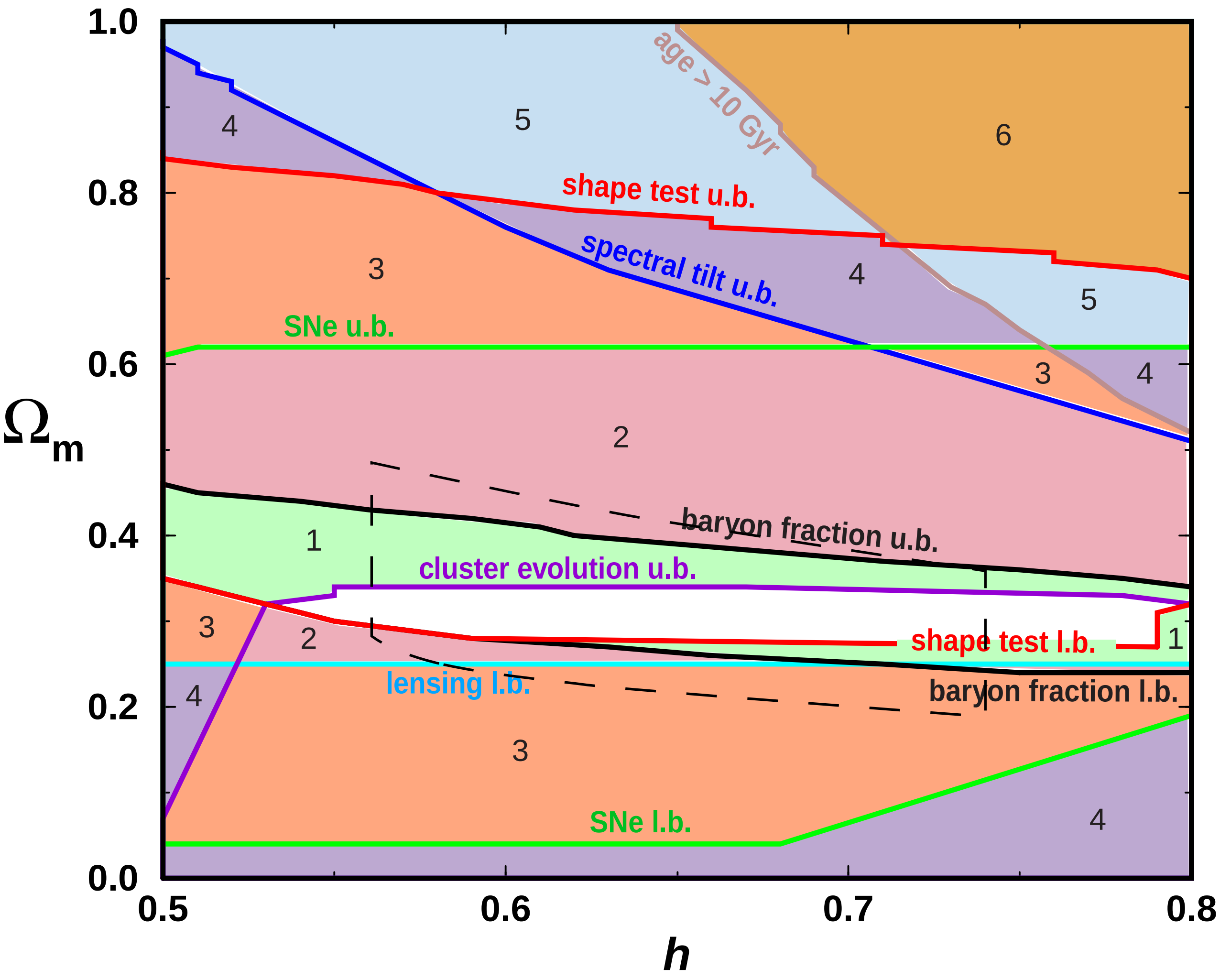

FIG. 15.— The concordance region (white) resulting if we artificially set $\Omega_b h^2 = 0.019$ and fix the spectral tilt to precisely match the central values of COBE normalization and cluster abundance measurements. The curves represent the constraints imposed by individual measurements. The curves divide the plane into patches which have been numbered (and colored) according to the number of constraints violated by models in that patch.

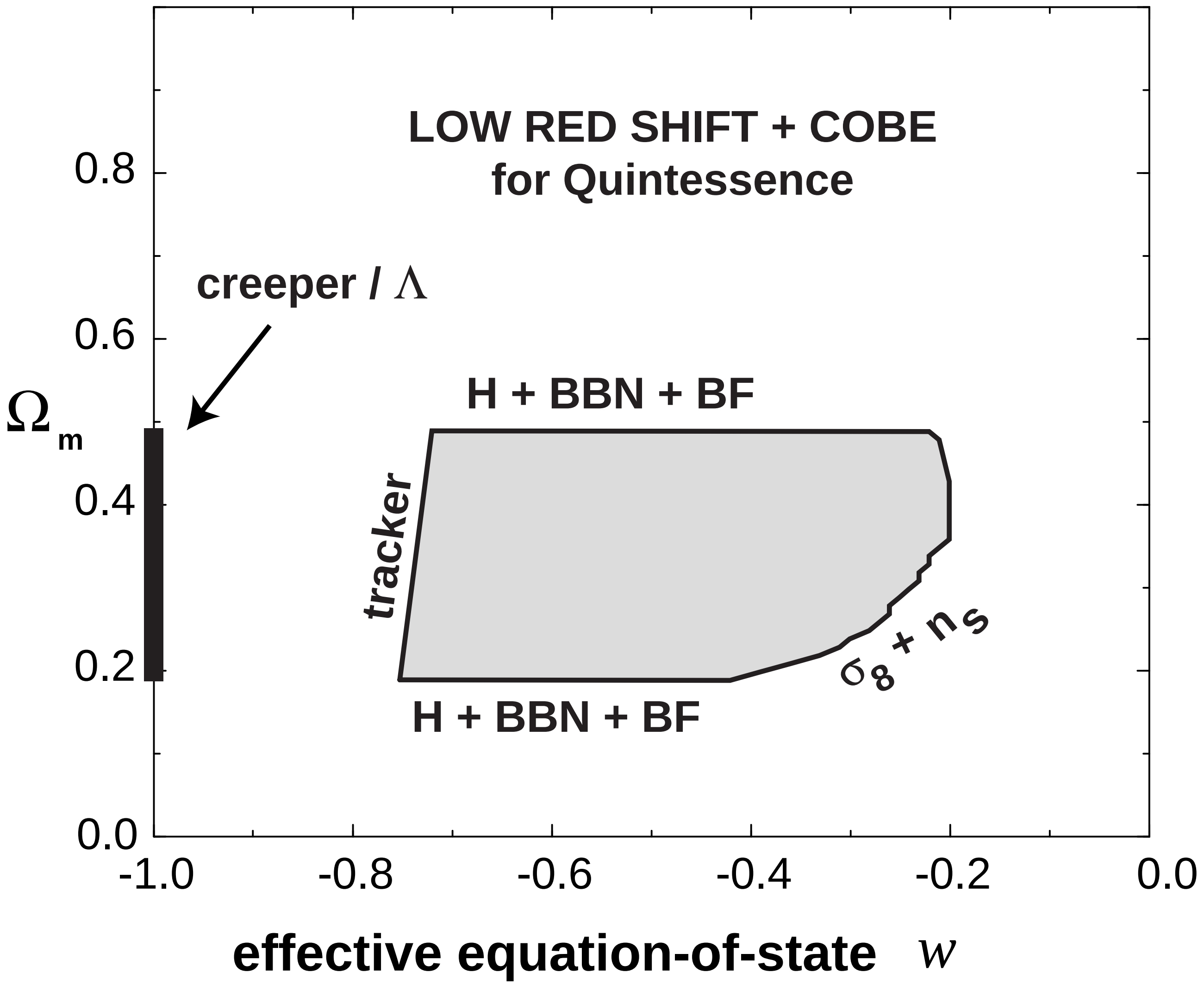

FIG. 16.— The concordance region based on COBE and low red shift tests for tracker quintessence is shown. The thin black swath along $w = -1$ shows the allowed region for creeper quintessence and Λ. The equation-of-state is time-varying; the abscissa is the effective (average) w.

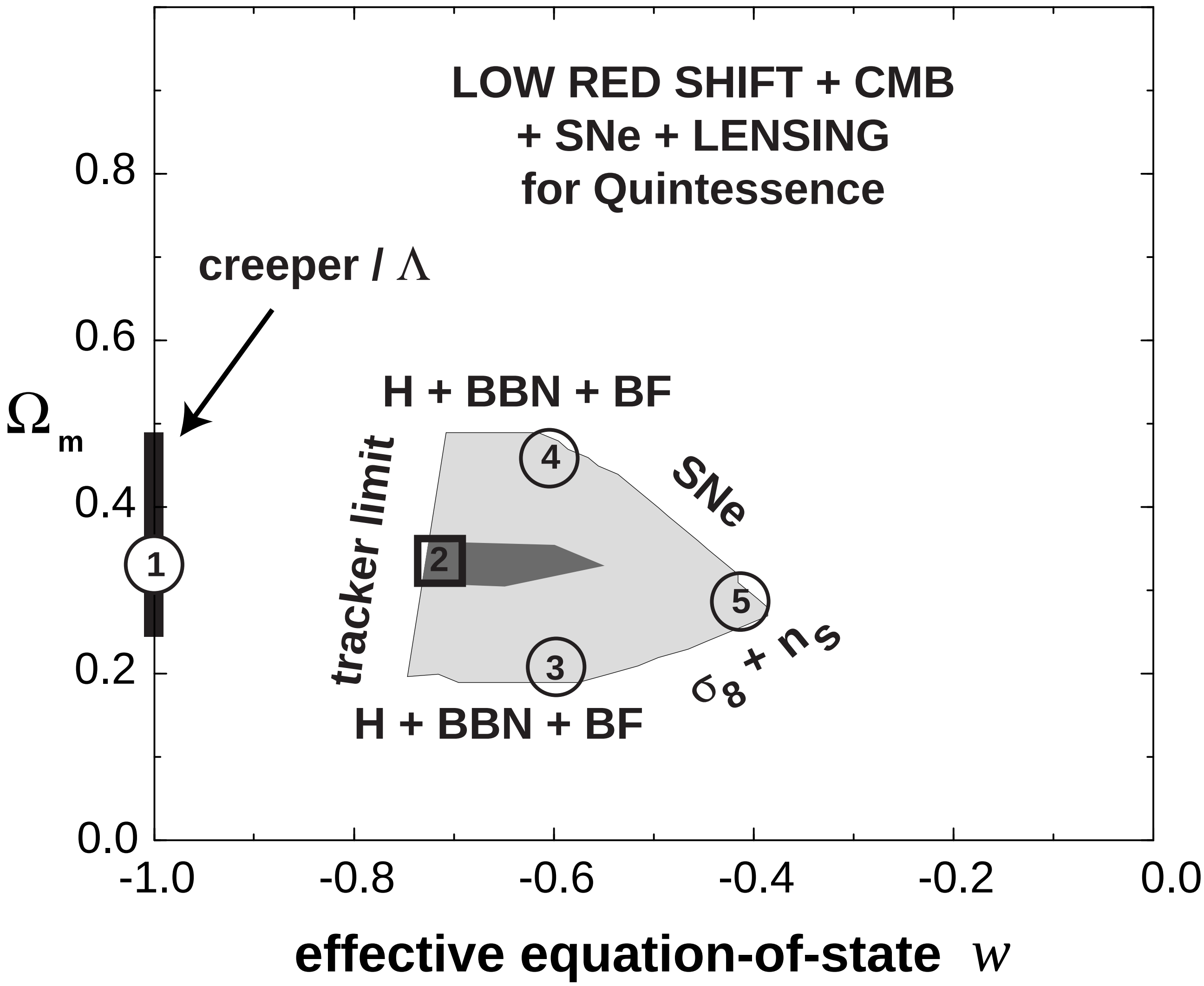

FIG. 17.— The overall concordance region based low, intermediate, and high red shift tests for tracker quintessence is shown. The thin black swath along $w = -1$ shows the allowed region for creeper quintessence and Λ. The equation-of-state is time-varying; the abscissa is the effective (average) w as defined in Eq. (3). The dark shaded region corresponds to the most preferred region (the 2σ maximum likelihood region consistent with the tracker constraint), $\Omega_m \approx 0.33 \pm 0.05$, effective equation-of-state $w \approx -0.65 \pm 0.10$ and $h = 0.65 \pm 0.10$ and are consistent with spectral index $n = 1$. The numbers refer to the representative models that appear in Table I and that are referenced frequently in the text. Model 1 is the best fit ΛCDM model and Model 2 is the best fit QCDM model.

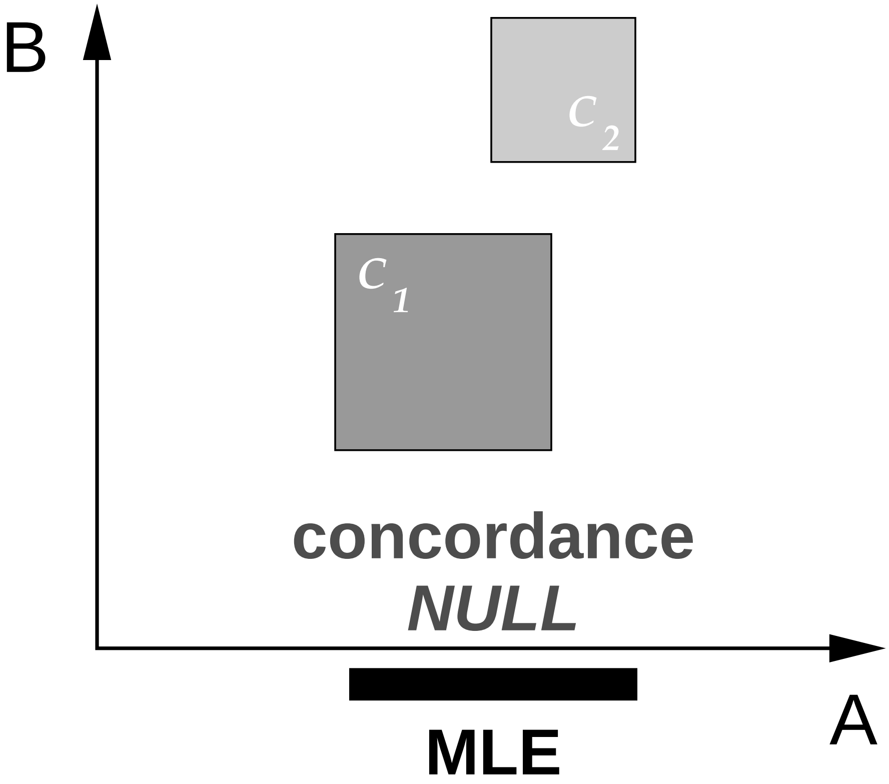

FIG. 18.— The constraint regions C_1 and C_2 do not intersect. In the concordance method for determining bounds on A, we first find the intersection of the C_1 and C_2 in the full, higher-dimensional parameter space, and then we project that intersection region to obtain the constraint on A. In this case, the concordance region is null. The MLE method always allows some finite region of 95%CL.

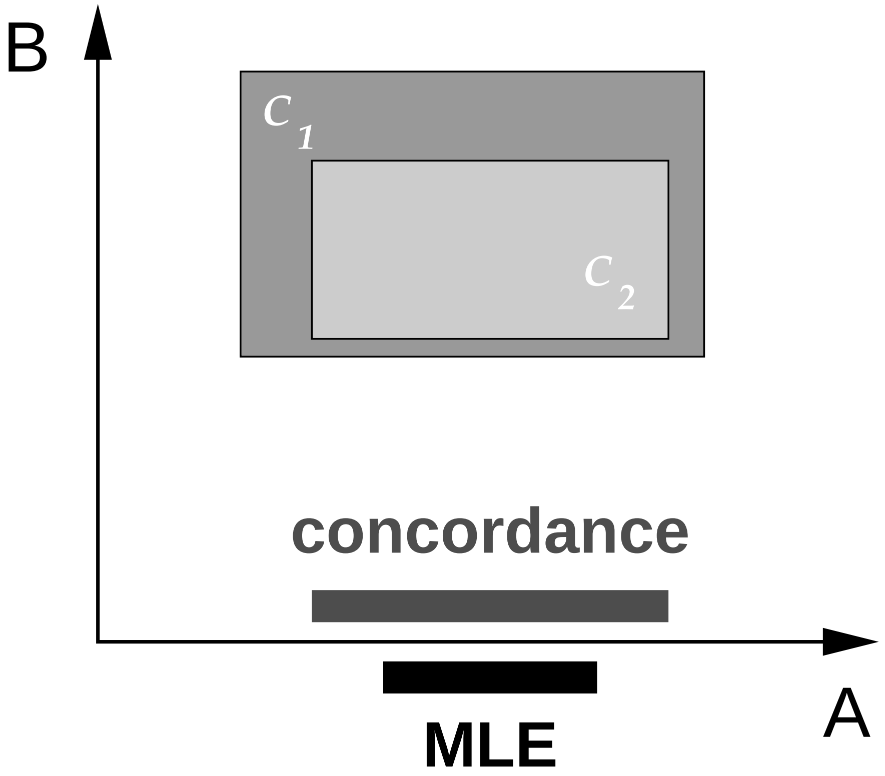

FIG. 19.— The constraint regions C_1 and C_2 overlap. The projection of the concordance and MLE regions onto parameter A, along the horizontal axis are shown by shaded strips.

		Model Parameters					Background Evolution Quantities							Fluctuation Spectrum Quantities				
model	#	w	Ω_m	h	Ω_b	n_s	t_0	$H_0 t_0$	q_0	$H_0 d_L\|_{z=1}$	dw/dz	$g(\Omega_m)$	$f(\Omega_m)$	$\delta_H \times 10^5$	σ_8	σ_{50}	v_{50}	v_{150}
creeper QCDM / ΛCDM	1	-1.0	0.33	0.65	0.041	1.0	14.1	0.94	-0.51	1.52	0.0	0.80	0.54	4.5	0.90	0.16	290^{+270}_{-200}	150^{+140}_{-100}
tracker QCDM	**2**	**-0.72**	**0.35**	**0.65**	**0.039**	**1.0**	**13.2**	**0.88**	**-0.20**	**1.44**	**0.063**	**0.74**	**0.55**	**4.1**	**0.83**	**0.15**	$\mathbf{260^{+240}_{-180}}$	$\mathbf{130^{+120}_{-90}}$
other QCDM	3	-0.60	0.20	0.80	0.025	1.2	11.7	0.96	-0.22	1.48	0.037	0.55	0.40	4.3	0.92	0.17	220^{+200}_{-150}	110^{+100}_{-80}
"	4	-0.60	0.44	0.60	0.056	1.0	13.4	0.82	0.0	1.36	0.057	0.76	0.63	3.4	0.80	0.13	260^{+240}_{-180}	130^{+120}_{-90}
"	5	-0.41	0.30	0.70	0.034	1.2	11.7	0.84	0.07	1.32	0.033	0.53	0.50	3.0	0.84	0.13	200^{+180}_{-140}	100^{+90}_{-70}
OCDM		—	0.33	0.65	0.045	1.3	12.0	0.80	0.17	1.39	—	0.48	0.52	1.8	0.89	0.13	200^{+180}_{-140}	100^{+90}_{-70}
SCDM		—	1.0	0.65	0.045	1.0	10.0	0.67	0.5	1.16	—	1.0	1.0	2.0	1.57	0.15	370^{+340}_{-260}	150^{+140}_{-100}

Table I: A set of representative quintessence models satisfying all concordance constraints. For models $\#2-5$, w is the effective equation-of-state. The age t_0 is in Gyr, while $H_0 t_0$ gives the age in units of the Hubble time, which is equivalently the instantaneous power at which the scale factor grows with time. The luminosity distance in units of the Hubble length is given by $H_0 d_L$ at red shift $z = 1$; this quantity is directly related to the distance modulus for supernovae. For comparison with the open, empty reference cosmology used in Figure 3, $H_0 d_L = 1.5$. The magnitude difference is then $\Delta(m-M) = 5\log_{10}(H_0 d_L/1.5)$. The rate of change of the equation-of-state for the tracker quintessence models, dw/dz, is evaluated at $z = 0$. The growth factor is defined as $g \equiv \delta/\delta_{scdm}$ and the growth rate is $f \equiv d\ln\delta/d\ln a$. The normalization of the mass power spectrum is given by δ_H, where $P(k) = \delta_H^2\, H_0^{3+n_s}\, k^{n_s}\, T^2(k)/(4\pi)$ and T is the baryonic and dark matter transfer function. The rms mass fluctuation excess, σ_8, σ_{50}, is evaluated for top hat window functions with radii 8, 50 Mpc/h. For the five representative models, σ_8 agrees with the cluster abundance constraint given in Eq. (5). Also, the values of $\eta_8 \equiv \sigma_8 \Omega_m^{0.6}$ as defined by Chiu et al. 1998 agree with their observational bound on η based on cluster abundances and peculiar velocities. The rms bulk velocity, in km/s, is evaluated for top hat radii of $R = 50$, 150 Mpc/h, with 2σ Maxwellian error bars. We have not listed any quintessence models located in the region excised between Figures 13 and 17 since models in this region are very similar to models 1 & 2. For comparison, the last two entries show the model parameters and properties of an open CDM model, and SCDM. The tilt of the open model is not based on a particular open inflationary model but has been chosen so that the model is both cluster and COBE (following Bunn & White 1997) normalized.